Shear Performance of ULCC and PCC: Experimental and Numerical Insights Using DIC and FEM

Yuyun Tajunnisa [1]*, Moh Safii Mansur [1], Priyo Suprobo [2], Auliagitta K. Apsari [1], Wahyuniarsih Sutrisno [2]

[1] Department of Civil Infrastructures Engineering, Institut Teknologi Sepuluh Nopember, Surabaya, Indonesia.

[2] Department of Civil Engineering, Institut Teknologi Sepuluh Nopember, Surabaya, Indonesia.

Abstract

This study investigates the shear behavior of reinforced concrete beams constructed with high-calcium fly ash-based Ultra-Low Carbon Concrete (ULCC) as a sustainable alternative to conventional Portland Cement Concrete (PCC). The objective is to assess ULCC's structural performance under shear and its potential as a low-carbon substitute. Using a dry-mix method with dry activators, six beams (five ULCC, one PCC) of identical dimensions ($150 \times 250 \times 1800$ mm) were tested under four-point bending, with variations in shear reinforcement, flexural reinforcement, and shear span-to-depth (a/d) ratios. Digital Image Correlation (DIC) was employed to monitor crack propagation and strain development, while Finite Element Modeling (FEM) provided numerical validation. Results show that increasing shear reinforcement enhanced capacity by 12.05%, whereas higher (a/d) ratios decreased it by 22.63%; increased flexural reinforcement improved shear resistance by 31.27%. FEM closely matched experimental outcomes, with a load-deflection ratio of 1.01. ULCC outperformed PCC in shear capacity and exceeded ACI 318-19 predictions. The integration of DIC and FEM offers a comprehensive analysis framework, and the findings demonstrate ULCC's viability as a structurally efficient, environmentally sustainable alternative for shear-critical applications.

Keywords: Ultra-Low Carbon Concrete (ULCC); Shear Behavior; Digital Image Correlation (DIC); Finite Element Modeling (FEM); Reinforced Concrete Beams; Sustainable Construction Materials.

1. Introduction

Concrete remains the most widely used construction material globally due to its versatility, durability, and cost-effectiveness. However, its environmental impact is a growing concern, particularly about the high carbon emissions associated with the production of Portland cement, which serves as the primary binder in conventional concrete. Cement manufacturing is responsible for approximately 5% of global carbon dioxide (CO_2) emissions [1, 2]. This significant contribution to global greenhouse gas emissions has placed the cement industry under increasing scrutiny, especially as global infrastructure development accelerates, resulting in growing demand for cement. [3]. Consequently, urgent efforts are needed to reduce cement consumption and promote more environmentally sustainable alternatives in the construction sector [4].

One promising strategy for reducing the carbon footprint of concrete is the development of cement-free binders through alkali-activated materials, commonly referred to as geopolymers [5-7]. Among these alternatives is Ultra-Low Carbon Concrete (ULCC), which utilizes aluminosilicate-rich industrial byproducts such as fly ash. These materials are

activated by alkaline solutions to produce a hardened binder that does not rely on Portland cement [8-10]. ULCC is categorized into two main types based on the calcium content of the fly ash used: low-calcium (Class F) and high-calcium (Class C) fly ash. Research on ULCC made with low-calcium fly ash has shown encouraging results in both micro- and macro-scale construction applications [11, 12].

Numerous experimental studies have evaluated the mechanical and structural behavior of ULCC elements produced using low-calcium fly ash and the wet mixing method [13]. For instance, investigations on columns have revealed that ULCC columns can outperform conventional OPC columns by up to 34% at the ultimate load stage [14]. These columns, like their OPC counterparts, tend to fail under compressive loading, with failure modes influenced by reinforcement ratios and eccentricity [15-17]. Additionally, the inclusion of steel fibers has been shown to significantly enhance compressive strength, increasing it by as much as 56% [18]. The addition of lateral confinement in ULCC columns has also been reported to improve both strength and ductility [19].

In the context of flexural elements, studies on ULCC beams have indicated that their behavior under bending loads is similar to that of OPC-based beams, especially when steel fibers are added to enhance flexural capacity by approximately 30% [20, 21]. Research on slabs made from ULCC has demonstrated that increasing thickness can improve stiffness and load-carrying capacity while reducing crack widths [22, 23]. Regarding shear behavior, experimental studies suggest that ULCC and OPC beams exhibit comparable performance, with no significant differences in shear capacity or failure modes [24-27].

Apart from experimental investigations, numerical modeling of ULCC structures has gained attention as a cost-effective and efficient tool for performance prediction. Finite Element Method (FEM) simulations using software like ATENA 3D have successfully modeled the behavior of ULCC beams under various loading conditions. For instance, a study involving nonlinear analysis of 37 ULCC beams showed that their flexural responses were comparable to OPC beams, with some models even demonstrating a 12% improvement in ductility [28-31]. These findings validate the potential of ULCC as a structurally viable and environmentally friendly alternative to conventional concrete.

Despite these advancements, the majority of existing ULCC research is centered around low-calcium fly ash and wet-mixing methods. High-calcium fly ash in geopolymer concrete remains limited due to certain drawbacks. One of the main challenges associated with high-calcium fly ash is its rapid setting time, which can hinder workability and complicate on-site construction operations [32, 33] To address this issue, researchers have explored the dry mixing method, which involves using solid alkaline activators instead of liquid ones. This approach has shown promise in extending the setting time to 150 minutes, thereby improving the practicality of using high-calcium fly ash in construction [34]. However, current research on this method has primarily focused on basic mechanical properties, with limited exploration of its structural performance under complex stress conditions, particularly shear.

Moreover, while the flexural behavior of ULCC beams has been extensively studied, the shear behavior of ULCC beams made with high-calcium fly ash using dry mixing methods has not yet been comprehensively examined. Understanding shear performance is critical for structural safety, as shear failures are typically brittle and occur without warning. Furthermore, few studies have integrated advanced diagnostic tools such as Digital Image Correlation (DIC) [35-38] , which can provide high-resolution analysis of full-field strain and crack patterns. When combined with validated FEM models, DIC offers a powerful means to analyze and compare experimental and simulated crack propagation.

Given these research gaps, this study aims to evaluate the shear behavior of reinforced ULCC beams produced using high-calcium fly ash and the dry-mixing method under various reinforcement and a/d ratios. The study employs four-point bending tests to examine load-deflection characteristics, crack development, and ultimate shear capacity. Additionally, Digital Image Correlation (DIC) is utilized to capture detailed crack patterns and strain fields, which are then compared to results from Finite Element Modeling (FEM) using validated numerical models. By integrating experimental and numerical analyses, this research contributes new insights into the feasibility of using dry-mixed, high-calcium ULCC for shear-critical applications, thus supporting its potential for broader industrial use as a sustainable structural material.

2. Material and Methods

This research was conducted through five sequential stages to investigate the structural behavior of reinforced geopolymer concrete beams using the dry mixing method. The results were further validated through numerical modeling based on the finite element method. The flowchart of the research methodology is presented in Figure 1. Each stage is described as follows:

- Stage 1: Collection and Testing of Constituent Materials

  The first stage involved the collection of materials required for geopolymer concrete production, including fly ash, alkaline activators (sodium hydroxide and sodium silicate), fine aggregates, coarse aggregates, and water. Each

material was tested to determine its physical and chemical properties, such as aggregate gradation, moisture content, specific gravity, and the chemical composition of fly ash. The results of these tests served as the basis for designing the concrete mix in the following stage.

- Stage 2: Mix Design Development

Based on the characterization results from Stage 1, a mixed design was developed for geopolymer concrete using the dry method. This process involved determining the optimal proportions of the constituent materials, including the activator ratio, water-to-binder ratio, and aggregate-to-paste ratio. Laboratory-scale trial mixes were conducted to achieve a mix that met the required mechanical strength and workability.

- Stage 3: Casting and Testing of Geopolymer Concrete (Dry Method)

After finalizing the mix design, the geopolymer concrete specimens were cast using the dry method. The fresh concrete was tested and then subjected to curing under controlled conditions. Mechanical performance was evaluated through compressive strength, split tensile strength, and flexural strength tests at selected curing ages (e.g., 7, 14, and 28 days) in accordance with relevant testing standards.

- Stage 4: Fabrication and Testing of Reinforced Geopolymer Concrete Beams

In this stage, reinforced concrete beams were fabricated using the geopolymer concrete mix previously developed. The beams were designed with specific dimensions and reinforcement details based on standard flexural testing procedures. After casting and curing, the beams were tested under flexural loading to evaluate their structural behavior, including maximum load capacity, deflection, crack pattern, and failure mode.

- Stage 5: Finite Element Modeling and Validation

The final stage involved modeling the beam structures using the finite element method with a 3D Nonlinear Finite Element Analysis (3D-NLFEA) software. The models replicated the experimental conditions, including geometry, material properties, loading, and boundary conditions. The simulation results—such as stress distribution, deformation, and crack propagation—were compared with the experimental data for model validation. This validation was essential to ensure the model's accuracy in representing the actual structural behavior and to enable its application in further parametric studies.
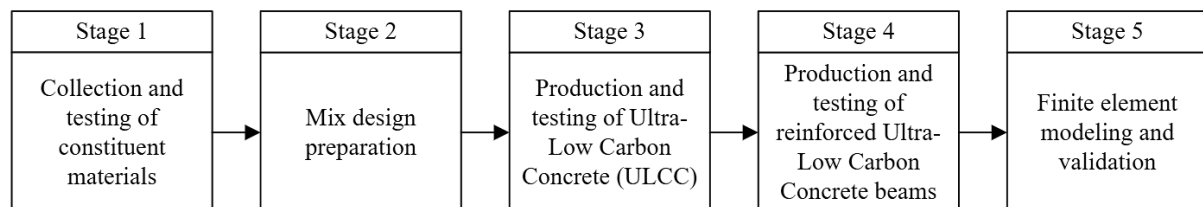
Stage 1	Stage 2	Stage 3	Stage 4	Stage 5
Collection and testing of constituent materials	Mix design preparation	Production and testing of Ultra-Low Carbon Concrete (ULCC)	Production and testing of reinforced Ultra-Low Carbon Concrete beams	Finite element modeling and validation

Figure 1. Methodology

2.1. Materials

The primary distinction between ULCC and conventional concrete lies in the binder, with all other ingredients remaining unchanged. Various tests were performed following ACI standards to determine the parameters and characteristics influencing the mix design formula for all material ingredients. These tested materials include fly ash, alkali activator, coarse and fine aggregates, and the tensile strength of the reinforcing steel. The results of these material tests are detailed in the subsection below.

2.1.1. Materials of ULCC

This research utilizes high-calcium fly ash as the primary cementitious material. The fly ash material was subjected to XRF and XRD testing in the laboratory. The fly ash XRF test results are presented in Table 1, while the XRD test results are in Table 2. The characterization of fly ash material was tested using the XRF (X-ray fluorescence) method to determine the type of fly ash that meets ASTM C-618 standards, as well as the XRD (X-ray diffraction) test to identify the crystalline and amorphous phases of the fly ash. Based on the test results, the material is classified as Type C fly ash (high-calcium fly ash) with a $SiO_2 + Al_2O_3 + Fe_2O_3$ content of 67.68% and a CaO content of 17.79%, by ASTM C618-19.

To determine the properties of the activators, Sodium Hydroxide (NaOH) and Sodium Metasilicate (Na_2SiO_3) were evaluated through specific gravity and gravimetric analyses, with the results presented in Tables 3 and 4, respectively. The specific gravity test for NaOH provides insight into its density relative to water, while the gravimetric analysis of Na_2SiO_3 reveals its sub-compound composition. Additionally, the characteristics of fine and coarse aggregates are summarized in Tables 5 to 12, covering parameters such as density, moisture content, absorption capacity, and particle size distribution. These data are crucial for the mix design of geopolymer concrete.

Table 1. XRF test result

Oxide Content (%)			
CaO	17.79	SO_3	1.39
SiO_2	37.94	K_2O	1.15
Al_2O_3	14.29	Na_2O	1.42
Fe_2O_3	15.45	TiO_2	0.84
MgO	7.12	P_2O5	0.18
LOI (%) 0.15			

Table 2. XRD test result

Solid Particles	Percentage (%)
Quartz	6.802
Brownmillerite (Si, Mg)	1.105
Periclase	3.748
C3A Na orthorhombic	0.463
C3A Cubic	1.106
C3A monoclinic	0.435
C3A Na Cubic	2.362
C3Aftrans	2.100
C3F (Colville)	0.676
Anhydrate	1.239
Magnetite	1.187
Spinel	1.819
Akermanite	0.001
Arcanite K2SO4	0.071
Lime	0.273
Maghemite	2.157
Ferrochrome	1.158
Amorphous	7.330

Table 3. Specific gravity test result

Parameters	Sample 1	Sample 2	Sample 3
Piknometer 1000 ml (gr)	248,4	266,9	265,6
NaOH (gr)	480	480	480
Piknometer + NaOH solution (gr)	1557,3	1613,4	1606,3
Specific gravity	1308,9	1346,5	1340,7
Average	**1332,03 kg/cm³**		

Table 4. Gravimetry test result

Na_2SiO_3			Total
H_2O	Na_2O	SiO_2	
46,44%	18,71%	21,7%	86,85%

Table 5. Sieve grading analysis of coarse aggregates

Num.	Restained weight	% Restained	Cumulative restained	% material passing
1 ½ "	0	0	0	100
¾ "	32,80	0,21	0,21	99,79
½ "	10240,00	64,11	64,32	35,68
3/8"	5353,00	33,51	97,83	2,17
Pan	346,30	2,17	100,00	0,00
Sum	15972,10	100,00	751,51	237,65
FKr			7,52 %	

Table 6. Coarse aggregates bulk density

Parameters	Sample A	Sample B	Sample C
Saturated Surface Dry (gr)	3000,2	3001,3	3000,8
Weight in the water (gr)	1894,6	1894,5	1891,2
Bulk density (gr/cm³)	2,714	2,712	2,704
Average bulk density		2,710 gr/cm³	

Table 7. The water absorption degree of coarse aggregates

Parameters	Sample A	Sample B
Saturated Surface Dry (gr)	3000,2	3001,3
Oven-dried weight (gr)	2954,5	2956,2
Water absorption degree	1,55%	1,53%
Average water absorption		1,54%

Table 8. Moisture content in coarse aggregates

Parameters	Sample A	Sample B
Aggregates	1001,7	1001,1
Oven-dried	986,6	984,8
Water moisture	1,53	1,65
Average moisture content		1,59%

Table 9. Sieve grading analysis of fine aggregates

Num.	Restained weight	% Restained	Cumulative restained	% material passing
4,76	0,3	0,03	0,03	99,97
2,38	38,1	3,82	3,85	96,15
1,19	156,3	15,68	19,53	80,47
0,6	148,6	14,91	34,44	65,56
0,3	332,8	33,39	67,83	32,17
0,15	251,7	25,25	93,08	6,92
0,075		0,00	93,08	6,92
Pan	69	6,92	100,00	0,00
Sum	996,8	100,00	311,84	388,16
FKr			3,12%	

Table 10. Fine aggregates bulk density

Parameters	Sample A	Sample B	Sample C
SSD fine agg (gr)	500,2	500,5	500,5
Measuring flask 1000 cc (gr)	265,7	248,5	265,7
Water and fine agg in the flask (gr)	1577,9	1561,1	1578,2
Water (gr)	1262,3	1241,7	1259,3
Spec grav of fine agg	2,709	2,763	2,756
Average of specific gravity 2,743 gr/cm³			

Table 11. The water absorption degree of fine aggregates

Parameters	Sample A	Sample B
Saturated Surface Dry (gr)	500,6	500,5
Oven-dried weight (gr)	499,6	500,3
Water absorption degree	0,20%	0,040%
Average water absorption	1,20%	

Table 12. Moisture content in fine aggregates

Parameters	Sample A	Sample B	Sample C
Aggregates (gr)	500,5	500,2	500,1
Oven-dried (gr)	469,5	470,9	470,4
Water moisture (%)	6,60	6,22	6,31
Average moisture content	6,38%		

The aggregates used in all types of beams have a gradation that matches the test results, as shown in Figures 2 and 3. The zone range was by ASTM C136 and applied to all the beam specimens.
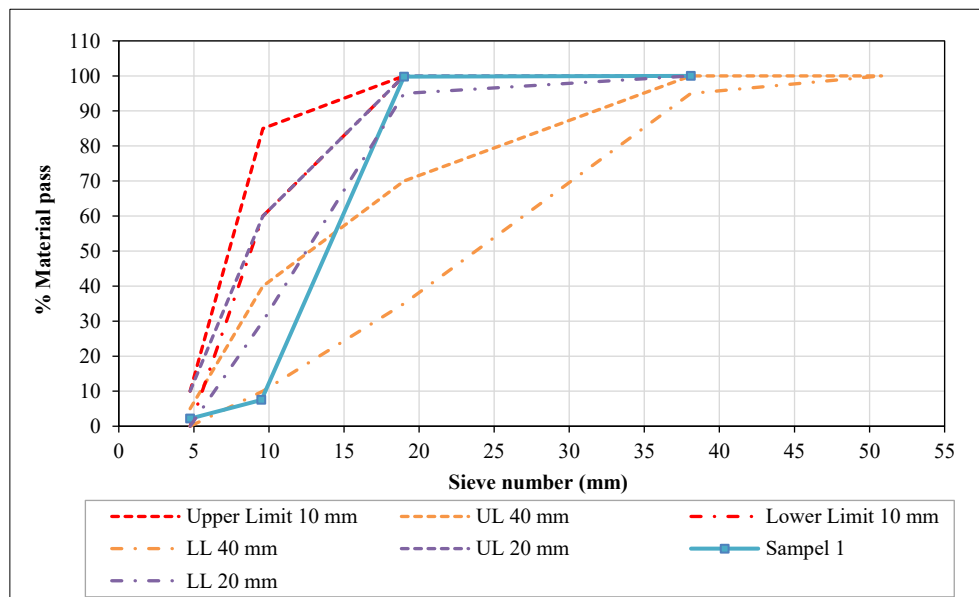
Figure 2. Sieve analysis graphic of coarse aggregates
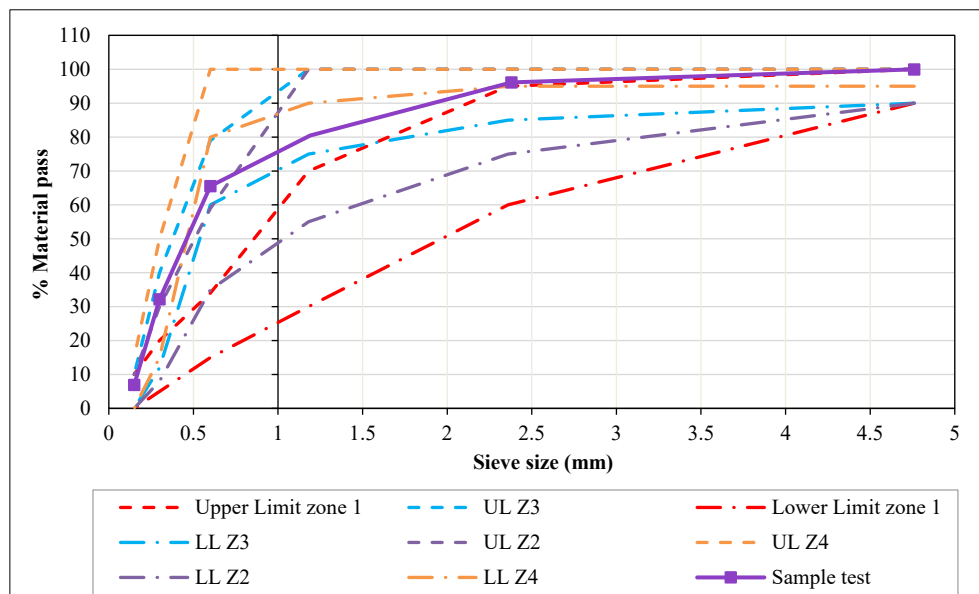
Figure 3. Sieve analysis graphic of fine aggregates

2.1.2. Reinforcing Steel Bars

The materials tested were a 16-diameter threaded reinforcing steel bar used for flexural reinforcement and a 6-mm diameter plain reinforcing steel bar used for beam shear reinforcement. Each reinforcing steel material consists of 3 rods with a length of 50 cm each, which are in Table 13. The results of testing the quality of reinforcing steel material with a diameter of 16 and a diameter of 6 are in Table 13. At the same time, Figure 4 shows two graphs depicting the stress-strain curves for two types of reinforcement bars: Bar D16 and Bar ø6. Each graph is divided into two subgraphs labeled (a) and (b), corresponding to different bars. Figure 4-a - Bar D16: This graph illustrates the stress-strain behavior of Bar D16, represented by three separate curves labeled D16-1, D16-2, and D16-3. Each curve shows how the stress in the bar increases with increasing strain until reaching a peak, after which the stress plateaus or slightly drops, indicating the yield point of the steel. The curves for D16-1, D16-2, and D16-3 are closely aligned, suggesting consistent material properties across different samples or testing conditions. Figure 4-b - Bar ø6 displays the stress-strain relationship for Bar ø6, with three curves labeled ø6-1, ø6-2, and ø6-3. These curves show a rapid increase in stress with strain, peaking at around 600 MPa before dropping off, indicating the material's yielding. The curves for ø6-1 and ø6-2 show similar patterns, while ø6-3 exhibits slightly different behavior, particularly in the post-peak region. Both graphs provide insights into the mechanical properties of the steel reinforcement bars used in construction, particularly their elastic and plastic behaviors.

Table 13. Reinforcement bar of D16 and ø6-1

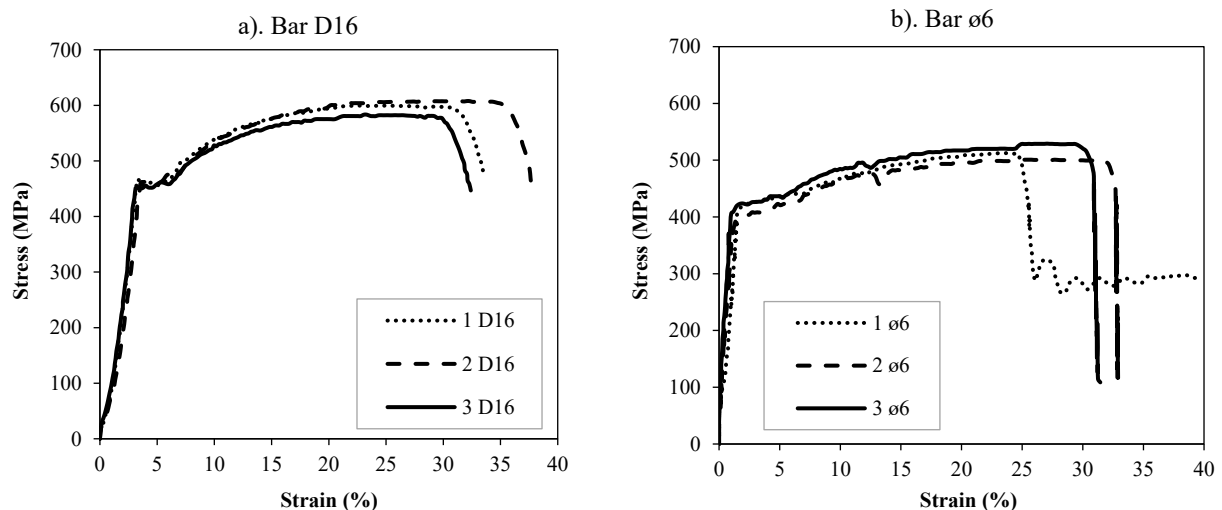| Type of Bar	Area (mm²)	Fy (MPa)	Fu (MPa)	Modulus Elastisitas (MPa)
Deform D16-1	193.92	481	614	200000
Deform D16-2	193.42	478	617	200000
Deform D16-3	192.93	473	615	200000
Mean	**193.42**	**477.33**	**615.33**	**200000**
Round ø6-1	24.55	489	595	200000
Round ø6-2	24.73	461	574	200000
Round ø6-3	24.99	480	588	200000
Mean	**24.76**	**476.67**	**585.67**	**200000**

Figure 4. Stress-strain reinforcement; (a) Bar D16, (b) Bar ø6

2.2. Mix Design

There are two steps in mix design calculation for ultra-low carbon concrete. At first, based on previous research by Phoo-Ngernkham et al. [39] with the determined molarity of the alkali solution, we get the material composition to create the desired compressive strength of the concrete. During the mixing process of this method, adding the alkali solution (NaOH and Na_2SiO_4) in a liquid state was reported to accelerate the setting time of the fresh concrete. This challenge is solved by converting the alkali solution into a solid state, considering the molarity. The mixing process is

different, although it resembles the usage of Ordinary Cement by the end. Using the ball-mill machine, the solid-state (flakes) alkaline was ground with fly ash to produce binder or geopolymer cement. This dry mixture was then packed and weighed to avoid any reaction with the open air and to control the proportion of the binder-aggregates composition. While mixing and casting, add the dry mixture with the aggregates, water, and superplasticizer. The fresh concrete made with this method is reported to have longer setting times and better workability.

2.2.1. Mix Design of ULCC

This study, 12 Molar NaOH was utilized as it provides the highest compressive strength with minimal standard deviation [40, 41]. The mix design in this research uses a formula developed by Phoo-Ngernkham et al. [39]. The recapitulation results of the ultra-low carbon concrete mix design using the wet method are presented in Table 14. These mixed design results will then be converted into the dry method.

Table 14. Mix design of ultra-low carbon concrete using the wet method.

Material	Amount (kg/m³)	2 % *Superplasticizer* (SP) of Fly ash content (kg/m³)
Fly ash type C	669.3	669.3
Fine aggregates	450	450
Coarse aggregates	1051.5	1051.5
NaOH	133.9	133.9
Na2SiO4	133.9	133.9
Superplasticizer	-	13.4
Concrete density	2438.5	2451.9

2.2.2. ULCC Mix Design Using Dry Mixing Method

Dry method conversion calculations refer to research [34, 42]. Mix design, as in Table 15 uses alkaline activator solutions. Then, the alkali activator in a solution was converted into a solid for the dry system method.

Table 15. Conversion of NaOH solutions

Molarity	Solid (gr)	Water (gr)	Solid/Fluid	Solid/ Water	Density NaOH (kg)
12 M	480	852	36%	56%	0.36

The mass of solid sodium hydroxide (NaOH) is calculated using the formula: NaOH solid = W OH x Ratio of Solid/Fluid. WOH represents the weight concentration of the solution, and the "Ratio of Solid/Fluid" is the percentage of solid NaOH in the mixture. WOH is 133.9 kg/m³, and the solid-to-fluid ratio is 36%. Applying these values to the formula yields 133.9 x 36%. This result indicates 48.2 kg of solid NaOH per cubic meter of solution. This calculation helps determine the concentration of NaOH in a solution, which is crucial for various industrial and laboratory applications where precise chemical composition is required.

Table 16 displays the gravimetric test results for a chemical compound, specifically sodium silicate hydrate (Na2SiO3·5H2O). The table lists the percentage by weight of each component within the compound: H2O (Water) is 46.44% by weight. This indicates that nearly half of the compound's mass is due to water, reflecting the hydrated nature of this sodium silicate. Na_2O (Sodium Oxide) is 18.71% by weight. Sodium oxide is a significant constituent, contributing to nearly a fifth of the compound's total mass. SiO_2 (Silicon Dioxide) is 21.70% by weight. Silicon dioxide forms a critical part of the structure, providing rigidity and network formation capabilities. This total is 86.85% by weight, the major constituents of the compound.

Table 16. The gravimetric test results for Na₂SiO₃.5H₂O

H2O	Na₂O	SiO₂	Total
46.44	18.71	21.70	86.85

Gravimetric analysis cannot analyze the remaining 39 elements in the $Na_2SiO_3.5H_2O$ fluid. The calculation for the mass of solid $Na_2SiO_3.5H_2O$ is, therefore, as follows:

$$Na_2SiO_3.H_2O_{solid} = \frac{wSi \times Na_2SiO_2}{Total} = \frac{133.9 \times (18.71+21.70)}{86.85} = 62.3 \text{ kg/m}^3 \tag{1}$$

1. The determination of water mass requirements

The determination of water mass is derived from the residual solid conversion present in each alkali activator.

a. The mass of water in the NaOH fluid

$$\text{Water NaOH} = W_{OH} - NaOH_{solid} = 133.9 - 48.2 = 85.7 \text{ kg/m}^3 \tag{2}$$

The result, 85.7 kg/m³, represents the mass of water per cubic meter in the NaOH solution. This indicates that out of the total mass of the solution, 85.7 kg/m³ is attributed to water.

b. The mass of water in the Na2SiO3.5H2O fluid

$$\text{Water } Na_2SiO_3.5H_2O = W_{SI} - Na_2SiO_3.5H_2O_{solid} = 133.9 - 62.3 = 71.6 \text{ kg/m}^3 \tag{3}$$

c. The total water content

$$\text{Water content} = \text{Water NaOH} + \text{Water } Na_2SiO_3.5H_2O = 85.7 - 71.6 = 157.3 \text{ kg/m} \tag{4}$$

The Equation 3 gives the formula for calculating the mass of water in the Na2SiO3.5H2O fluid. In this formula, WSI represents the total mass of the solution per cubic meter, and Na2SiO3.5H2O solid represents the mass of solid Na2SiO3.5H2O per cubic meter. WSI=133.9 kg/m³ indicates the total mass of the $Na_2SiO_3.5H_2O$ solution. The mass of water, referred to Equation 4, is then calculated by subtracting the mass of solid Na2SiO3.5H2O from the total mass of the solution. There is an additional step where the water content from two different sources or solutions is combined: the previously calculated water mass from another solution, 85.7 kg/m³, is added to the 71.6 kg/m³ from the $Na_2SiO_3.5H_2O$ solution. The total combined water content is 157.3 kg/m³, indicating the cumulative mass of water per cubic meter from both solutions, reflecting the aggregate water composition in the overall mixture or two combined processes.

2. Recapitulation of a mixed design using the dry method

The recapitulation results of the ultra-low carbon concrete mix design for conversion from the wet method to the dry method are presented in Table 17. This mix design is used in making cylindrical specimens and reinforced concrete beams.

Table 17. Recapitulation of the dry method ultra-low carbon concrete mix design

Material	Amount (kg/m³)
Fly ash type C	669.3
Fine aggregates	450
Coarse aggregates	1051.5
12 M NaOH	48.2
$Na_2SiO_3.5H_2O$	62.3
Water	157.3
Superplasticizer	13.4
Concrete density	2451.9
W/C	0.2

2.3. Specimens Preparation

2.3.1. Specimen Details of Beam

To induce shear failure in reinforced concrete beams, flexural reinforcement must exceed shear strength, with moment capacity (Mn) based on longitudinal reinforcement and shear capacity (Vn) on stirrups, per ACI 318. Table 18 presents detailed information about six concrete beam specimens used in this study, outlining top and bottom reinforcement, stirrups, and shear span-to-depth ratios (a/d). All beams have two ø6 bars at the top, while bottom reinforcement varies to two or three D16 bars (e.g., G2B2). The stirrups differ between ø6-200 mm and ø6-250 mm spacing or are absent (G1C2). Spacing was designed to yield Vn < Mn, encouraging shear failure. The differences in stirrup spacing aim to access shear reinforcement effects. Most beams have an a/d of 2, except G1B2.5 (a/d = 2.5), indicating a longer shear span. "G" denotes ULCC, and "P" denotes PCC. Figure 4 shows the beam cross-section.

Table 18. Specimen beams

No.	Beam	Longitudinal Reinforcement		Stirrups	a/d
		Top	Bottom		
1	G1A2	2 ø6	2 D16	ø6 – 200	2
2	G1B2	2 ø6	2 D16	ø6 – 250	2
3	G1B2.5	2 ø6	2 D16	ø6 – 250	2.5
4	G2B2	2 ø6	3 D16	ø6 – 250	2
5	G1C2	2 ø6	2 D16	-	2
6	P1B2	2 ø6	2 D16	ø6 – 250	2

Note: G: Ultra-low carbon concrete (ULCC); P: Portland Cement Concrete (PCC)

The purpose of comparing various specimens, as shown in Table 18, Figures 5 and 6 is outlined as follows:

- Beams G1A2, G1B2, and G1C2 were analyzed to assess how shear reinforcement influences shear strength.

- Beams G1B2 and G1B2.5 were evaluated to explore the impact of the shear span-to-depth ratio (a/d) on shear strength.

- Beam G1B2 and G2B2 were examined to understand the effect of varying flexural reinforcement on shear strength.

- Beam G1B2 and P1B2 were compared to investigate the differences in shear strength between Ultra-low Carbon Concrete (ULCC) and Portland Cement Concrete (PCC).
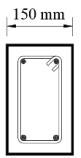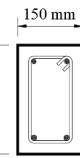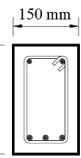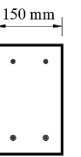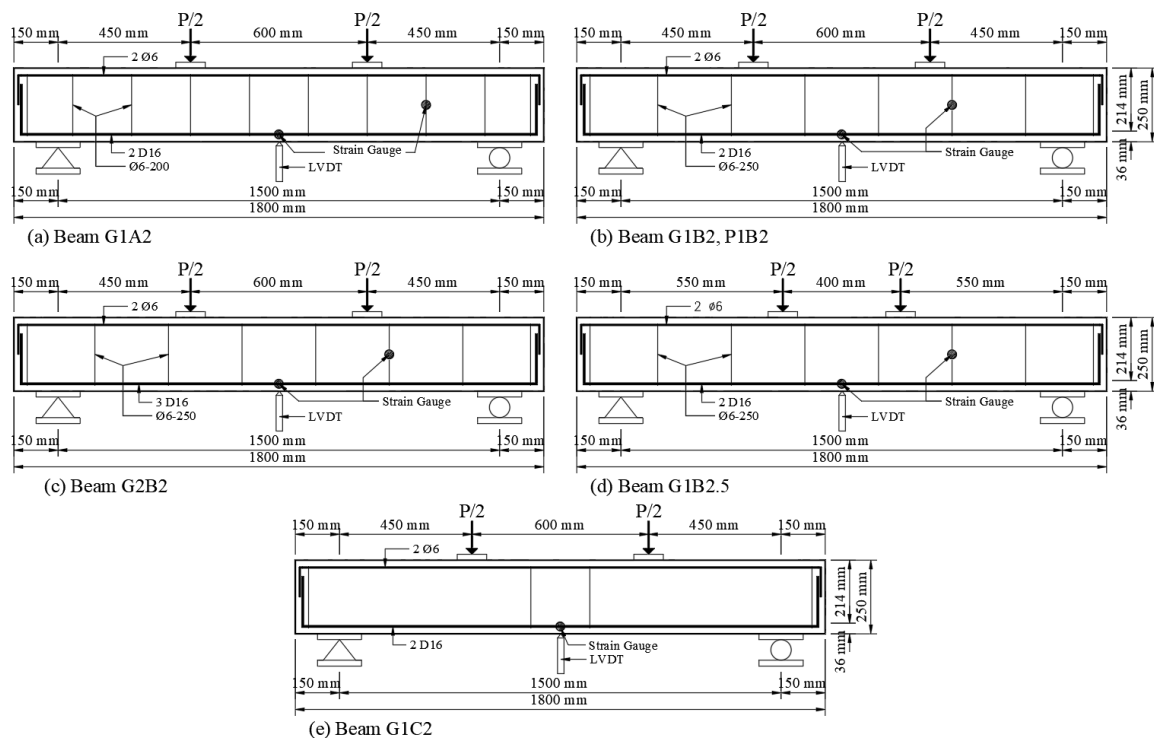

Figure 5. Cross-section specimen beams

Figure 6. Long-section specimen beams

Figure 6 depicts schematic diagrams of six different reinforced concrete beam configurations, each annotated with specific dimensions and structural details to illustrate experimental setups used in structural engineering research. Each beam is labeled to indicate the specific experimental variable under study. Beam G1A2: This figure shows a beam with two primary loads applied at two equally spaced points. The beam includes strain gauges and a Linear Variable Differential Transformer (LVDT) for measuring deflection and strain. The beam uses two reinforcement bars (D16) along its bottom and a thinner reinforcement along the top (2 ø6). Beam G1B2, P1B2: Similar to the structural setup of beam G1A2, this beam also includes point loads divided symmetrically and features strain gauge and LVDT placements for data collection. It uses similar reinforcement with two D16 bars at the bottom. Beam G2B2 alters the placement of the load points slightly closer together than G1A2, reducing the span between them. It uses three D16 bars at the bottom for reinforcement and maintains the strain gauge and LVDT for measurements. Beam G1B2.5: This variant adjusts the load positions, creating a wider central span with the two-point loads located further from the beam's center. It uses two D16 bars at the bottom for reinforcement. Beam G1C2: This setup presents a standard configuration with two symmetrically placed point loads, two bottom D16 reinforcements, and a top reinforcement. It includes a strain gauge and an LVDT, similar to other configurations. The configurations are carefully designed to test different aspects of beam behavior under load, such as the effects of shear and flexural reinforcement, load distribution, and the structural response of different materials (as indicated by the labels like ULCC and PCC). The consistent inclusion of strain gauges and LVDTs across the beams suggests a focus on accurately measuring deformation and stress response under applied loads.

2.3.2. Fabrication and Curing

The beam formwork used in this research uses aluminum materials. Aluminum is used as formwork because it has advantages compared to steel: it does not rust easily and is not sticky to ULCC. The formwork size corresponds to the planned beam, namely 150×250 mm with a length of 1800–2400 mm, which can be adjusted to suit the beams. Figure 7 shows one reinforced concrete beam formwork using aluminum material supported with 3 L30.30.3 elbows. The purpose of using elbows is to strengthen the formwork so that it does not experience deflection when casting concrete.

Figure 7. Beam formwork

Concrete curing is carried out in an open room with exposure to surrounding air, called ambient curing. The ambient air temperature conditions are 33+3°C with a humidity of 53+5%. Figure 8 shows the curing of ULCC beams with exposure to ambient air. The beams are covered with tarpaulin to prevent environmental weather.

Figure 8. The curing process of the beam specimens

2.4. Test Method

2.4.1. Slump Test

The slump test is carried out to determine the consistency or stiffness of the fresh concrete mixture used to assess the concrete's workability level. The higher the slump value will be directly proportional to the concrete's workability level. As shown in Figure 9, the test yielded a slump value of 200 ± 20 mm, indicating a high level of workability suitable for applications requiring ease of placement.

Figure 9. Slump test of the ULCC

2.4.2. Compressive Strength

Table 19 shows the results of compressive strength testing for cylindrical-ultra-low carbon concrete and PCC concrete specimens derived from six different beam groups, each labeled from G1A2 to P1B2. For each group, three-cylinder specimens were tested to determine average compressive strength values. Among all the beam groups, the highest average compressive strength was recorded for specimen group G1B2.5, with a mean value of 59.80 MPa. This was followed closely by group G1B2 at 58.23 MPa and G1C2 at 58.19 MPa, suggesting that these mixes provided consistently high strength and quality. On the other hand, the lowest compressive strength was observed in group Portland Cement Concrete P1B2, with an average of only 32.59 MPa. This discrepancy is attributed to differences in mix composition, curing conditions, or possible inconsistencies during specimen preparation. The low compressive strength in the concrete mixture using ordinary Portland cement is due to the difficulty in achieving high strength with cement-based materials. This study challenges in optimizing the mix, which may include an inadequate water-to-cement ratio, limited cement hydration, or less-than-ideal curing conditions. Without supplementary materials or admixtures, reaching higher strength levels can be difficult.

Table 19. Compressive strength

No.	Beam	No Cylinder	W (kg)	F (kN)	Density (kg/m²)	Fc (MPa)	Fc mean (MPa)
1	G1A2	1	3.94	457	2508.28	58.19	51.57
		2	3.86	398	2457.35	50.67	
		3	3.98	360	2533.75	45.84	
2	G1B2	1	3.98	454	2533.75	57.81	58.23
		2	4.00	464	2546.48	59.08	
		3	4.02	454	2559.21	57.81	
3	G1B2.5	1	3.98	461	2533.75	58.70	59.80
		2	3.88	480	2470.08	61.12	
		3	4.02	468	2559.21	59.59	
4	G2B2	1	3.90	479	2482.82	60.99	57.68
		2	3.98	448	2533.75	57.04	
		3	3.98	432	2532.61	55.00	
5	G1C2	1	3.90	426	2482.82	54.24	58.19
		2	3.92	486	2495.55	61.88	
		3	3.90	459	2482.82	58.44	
6	P1B2	1	3.90	257	2482.82	32.72	32.59
		2	3.88	274	2470.08	34.89	
		3	3.86	237	2457.35	30.18	

The densities of the concrete samples remained relatively consistent across all groups, ranging from approximately 2457 kg/m³ to 2559 kg/m³, reflecting uniform material quality in terms of mass per volume. However, variations in compressive strength within some groups, such as in G1A2 where values ranged from 45.84 MPa to 58.19 MPa, indicate variability in compaction or curing efficiency. Overall, the data demonstrate the influence of mix design and quality control on the mechanical performance of concrete, particularly in terms of compressive strength.

2.4.3. Shear Performance Test

The beam shear test uses a two-point load. Six beams are tested and have dimensions of 1800 mm, a height of 250 mm, and a width of 150 mm, according to Table 18. The compressive strength of each beam type is in Table 19. Each test specimen to be subjected to shear testing must be prepared in advance. The beams are marked for the placement of the support points at the roll joints. Additionally, markings are made for the placement of the load points.

Figure 10 shows the testing of ultra-low carbon concrete (ULCC) and Portland cement concrete (PCC) beams. A rolling bed with a precise beam length of 1500 mm is used to test each beam. A hydraulic jack with a 50-psi capacity is used for loading, and a load cell with a 1000 kN capacity is used for load measurement. Deflection measurements will also be taken at the mid-span and directly beneath the two-point load using LVDTs with 100 mm and 50 mm capacity. The TDS-630 Data Logger will read the load cell, LVDT data, and strain gauge data installed on the longitudinal and shear reinforcement.

Figure 10. Set up four-point bending testing

Figure 11 illustrates the DIC camera setup: Figure 11-a depicts the camera placement locations, while Figure 11-b shows the layout for capturing images on each side of the reinforced concrete beam during testing. The cameras were positioned on the right and left sides of the beam being tested. The cameras utilized for this experiment were a Canon 600D and a Canon 700D. Image capture was automated using Magic Lantern software installed on the cameras, with images taken at intervals of 5 seconds per frame. These images were subsequently analyzed using GOM Correlate software.
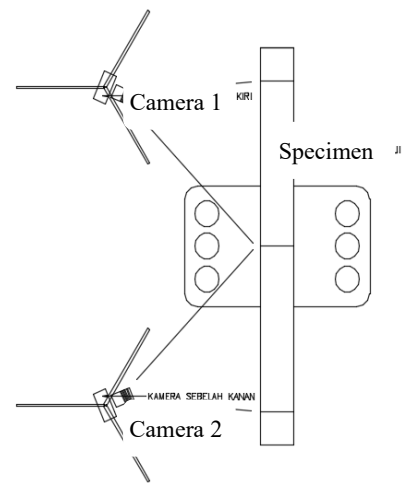

Figure 11. Setup for DIC camera measurements: (a) Camera placement location, (b) Camera placement layout.

2.5. Finite Element Analysis

At this stage, finite element modeling of both geopolymer concrete beams and conventional Portland cement concrete (PCC) beams is performed using a three-dimensional nonlinear finite element analysis (3D-NLFEA) program [43-49]. Prior to simulating the beams based on the experimental results obtained in this study, an extensive literature review is conducted to establish reliable modeling parameters and strategies. Furthermore, the numerical modeling approach is validated against previously published experimental data to ensure accuracy and consistency. The validation process refers to the study conducted by Yacob et al. [25] which serves as a benchmark for assessing the reliability of the developed finite element model.

2.5.1. 3D-NLFEA Modeling Procedure

2.5.1.1. Pre-Processor

The pre-processing stage involved geometric modeling and input preparation using SALOME 9.3.0 and Microsoft Excel with Visual Basic for Applications (VBA). The steps conducted during the pre-processing stage included:

1. *Geometric Modeling*

   The beam geometry consisted of concrete elements, reinforcing steel bars, steel support plates, and steel loading plates.

2. *Boundary Conditions*

   Boundary conditions were defined to replicate the actual experimental setup. These included specifying the locations of supports and loading points on the model elements.

3. *Meshing*

   The mesh discretization process subdivided the model into smaller finite elements. For concrete and solid steel plates, 3D extrusion elements were used, while wire discretization was applied for reinforcing bars. A mesh size of 25 mm was adopted. The meshed model was exported into nodal format to be used in the next stage.

4. *Input of Material Properties*

   The output of the SALOME pre-processor, in the form of node definitions, was used to assign material properties and boundary conditions through Microsoft Excel as an input for the 3D-NLFEA program.

2.5.1.2. Nonlinear Analysis

The nonlinear finite element analysis was performed using the 3D-NLFEA program. During this process, the load–displacement (P–Δ) response of the beam could be monitored in real time on the computer interface.

2.5.1.3. Post-Processor

The post-processing stage enabled a detailed evaluation of the structural behavior of the modeled elements. Visualization and interpretation of the simulation results—such as stress distribution, cracking patterns, and deformation—were conducted using ParaView software.

2.5.2. Analysis of Experimental and Numerical Results

At this stage, both the experimental and numerical results were analyzed and compared. The primary aspects assessed in the analysis included:

- Shear capacity of the beam;
- Structural deformation behavior;
- Crack patterns and propagation.

3. Results and Discussions

3.1. Analysis of Previous Studies of ULCC Beam

Model validation is a necessary step prior to conducting structural modeling based on the experimental results obtained in this study. The material and geometric models used to validate the 3D-NLFEA program in analyzing the shear behavior of geopolymer concrete beams refer to the study by Yacob et al. [25].The material properties adopted for the validation process are presented in Table 20. The type of geopolymer concrete beam used for model validation is the GL6-2 beam, as illustrated in Figure 12.

Table 20. Material Properties of Reinforced Geopolymer Concrete Beam Type GL6-2 [25]

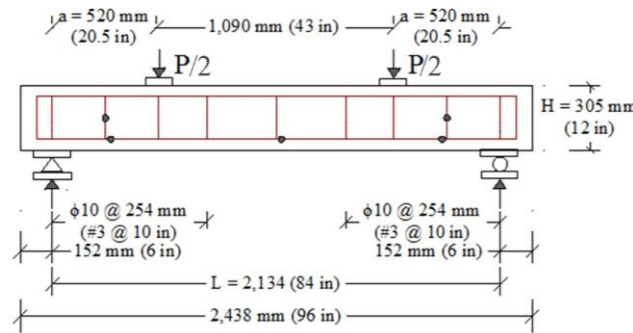| Parameter	Value	Unit
f^o_{cu}	43.4	MPa
f^o_t	2.15	MPa
Ec	30,000	GPa
fy D19	561	MPa
fy D10	490	MPa

Figure 12. Dimensions of GL6-2 and CL6-2 Beam Types [25]

3.1.1. Validation of Peak Load–Deflection Results

The peak load–deflection curve obtained from the 3D-NLFEA modeling is presented in Figure 13. The results indicate that the curve generated by the 3D-NLFEA model is higher than the experimental results reported by Yacob et al. [25]. This discrepancy may be attributed to the significant variability in concrete material properties. In this study, the constitutive model developed by Piscesa et al. [48] was adopted. [50] stated that the size and composition of aggregates can influence fracture energy, initial microcracks, and overall concrete strength. Moreover, curing conditions also play a role in affecting the material behavior of tested beams. Although the material model used in this numerical simulation was carefully adapted to match the actual conditions, the constitutive model by Piscesa et al. [48] inevitably differs from the real conditions observed during experimental testing. These factors likely contribute to the differences between the numerical and experimental results.
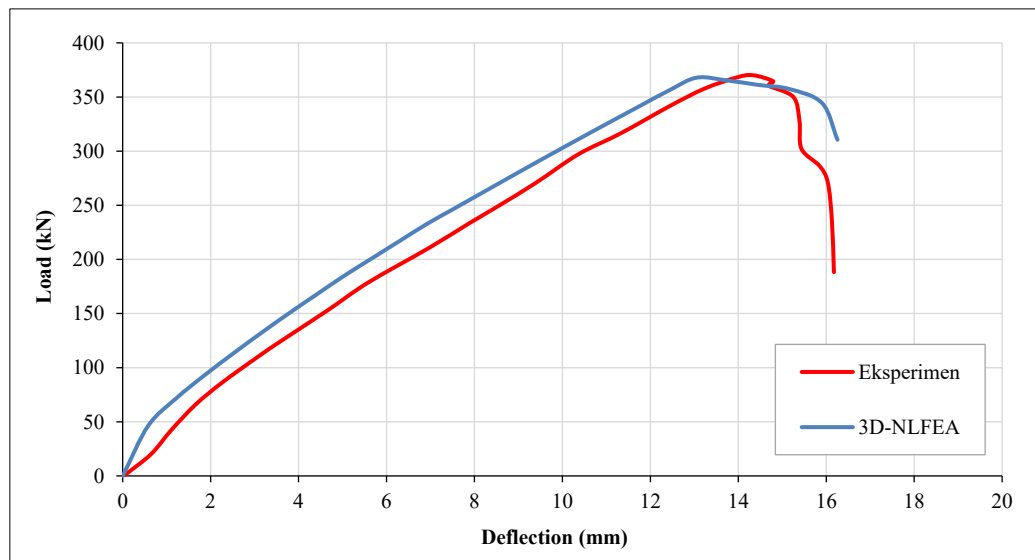

Figure 13. Peak Load–Deflection Curve of GL6-2 Beam: Experimental vs. 3D-NLFEA Results

The peak load–deflection curve of the geopolymer concrete beam from the experiment showed a peak load of 372 kN, while the peak load obtained from the 3D-NLFEA model was 368 kN, resulting in a Pu Test / Pu 3D-NLFEA ratio of 1.01. For mid-span deflection of the GL6-2 geopolymer concrete beam, the experimental result was 17 mm, whereas the deflection from the 3D-NLFEA simulation was 16 mm, yielding a deflection ratio (Disp. Test / Disp. 3D-NLFEA) of 1.06. A summary of the validation results for peak load and deflection is presented in Table 21.

Table 21. Comparison of Peak Load and Deflection: Experimental Results vs. 3D-NLFEA Analysis

Beam	Ultimate Load			Midspan Displacement		
	Pu Test (KN)	Pu 3D-NLFEA (KN)	Pu Test / Pu 3D-NLFEA	Disp Test (mm)	Disp 3D-NLFEA (mm)	Disp Test / Disp 3D
GL6-2	372	368	1.01	17	16	1.06

3.1.2. Validation of Shear Capacity

The shear force obtained from previous experimental research [25] was compared with the shear force results generated by the 3D-NLFEA program and the Response 2000 software developed by Bentz [51]. In addition, the

experimental shear force was also compared with analytical calculations based on the ACI 318-19 code. A comparison of the experimental shear results with those from 3D-NLFEA, Response 2000, and ACI 318-19 is presented in Table 22.

Table 22. Comparison of Shear Force Results: Experimental vs. 3D-NLFEA, Response 2000, and ACI 318-19

Beam	Shear Load						
	Vu Test (KN)	Vu 3D-NLFEA (KN)	Vu Response 2000 (KN)	Vn ACI 318-19 (KN)	Vu Test / Vu 3D-NLFEA	Vu Test / Vu Response 2000	Vu Test / Vn ACI 318-19
GL6-2	186	184	190.6	177.67	1.01	0.98	1.05

Based on the results presented in Table 22, it can be observed that the GL6-2 beam type has a Vu Test / Vu 3D-NLFEA ratio of 1.01, with the experimental shear force (Vu Test) recorded at 189 kN and the 3D-NLFEA shear force (Vu 3D-NLFEA) at 184 kN. Meanwhile, the comparison between the experimental shear force and the Response 2000 analysis shows a Vu Test / Vu Response 2000 ratio of 0.98, with Response 2000 predicting a shear force of 190.6 kN. Additionally, the experimental shear force was compared with the shear capacity calculated according to the ACI 318-19 code. The Vu Test / Vn ACI 318-19 ratio is 1.05, with the ACI 318-19 calculated shear capacity (Vn) being 177.67 kN. These results indicate that the ACI 318-19 calculation is more conservative, reflecting the safety considerations inherent in structural design.

3.2. Load Deflection Behavior

Based on the test results of reinforced concrete beams in Figure 14 and Table 23, the G2B2 type beam has the highest peak load value of 302.02 kN. Then proceed with beams of type G1B2, G1A2, G1C2, and G1B2.5, which have values of 230.07 kN, 208.67 kN, 202.36 kN, and 178.01 kN, respectively. Meanwhile, the beam with the smallest peak load value is the P1B2 type beam, which is 130.71 kN.
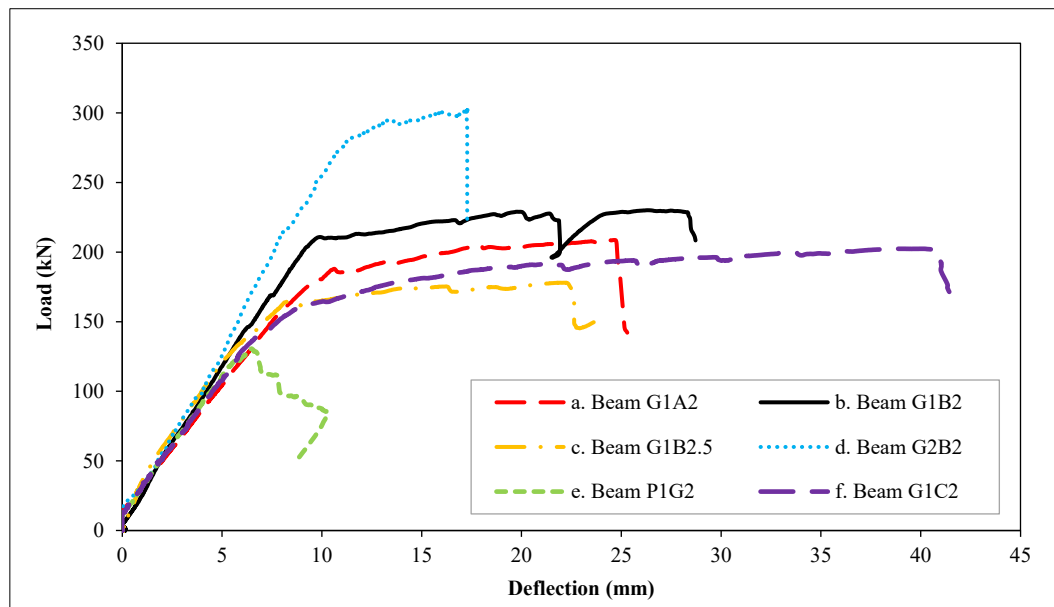

Figure 14. Load mid-span deflection response of the beam specimens (a) G1A2, (b) G1B2, (c) G1B2.5, (d) G2B2, (e) P1G2, and (f) G1C2

Table 23. Peak load and mid displacement test result

No.	Beam	Fc' (MPa)	Reinforcement			a/d	Ultimate Load	
			Top	Bot	Stirrups		Pu Test (kN)	Mid. Disp. Test (mm)
1	G1A2	51.57	2 ø6	2 D16	ø6 – 200	2	208.67	25.30
2	G1B2	58.23	2 ø6	2 D16	ø6 – 250	2	230.07	28.72
3	G1B2.5	59.80	2 ø6	2 D16	ø6 – 250	2.5	178.01	23.64
4	G2B2	57.68	2 ø6	3 D16	ø6 – 250	2	302.02	17.32
5	G1C2	58.19	2 ø6	2 D16	-	2	202.36	41.46
6	P1B2	32.59	2 ø6	2 D16	ø6 – 250	2	130.71	10.32

The experimental results presented in Table 23 highlight the interplay between concrete compressive strength, reinforcement configuration, and the shear span-to-depth (a/d) ratio in influencing the ultimate load capacity and displacement behavior of reinforced concrete beams. Beams with higher compressive strength generally exhibited greater peak loads, as observed in specimens G1B2.5 and G2B2, which had compressive strengths exceeding 57 MPa and peak loads above 178 kN. However, the relationship is not solely linear, as reinforcement detailing also plays a critical role. For example, G2B2, with adequate stirrup spacing (φ6–250 mm) and an a/d ratio of 2, showed the highest peak load of 302.02 kN, outperforming G1B2.5 despite the latter having slightly higher compressive strength. This outcome suggests that shear reinforcement and geometric configuration significantly contribute to overall beam strength.

The a/d ratio also demonstrated a notable influence on beam behavior. Beam G1B2.5, the only specimen with an a/d ratio of 2.5, exhibited a reduced load capacity of 178.01 kN compared to other specimens with an a/d ratio of 2. This reduction is consistent with established structural theory, where higher a/d ratios result in more flexure-dominated failure and reduced shear resistance. The influence of stirrup confinement on ductility was also evident. Beams with properly spaced stirrups demonstrated higher mid-span displacements, indicating better energy absorption and post-peak deformation capacity. Conversely, beam P1B2, with the lowest compressive strength and standard stirrups, showed brittle failure at a peak load of 130.71 kN with limited displacement (10.32 mm). This brittle behavior confirms the vulnerability of low-strength concrete in structural elements under flexural and shear stress.

Interestingly, beam G1C2, which lacked shear reinforcement (stirrups), reached a moderate ultimate load (202.36 kN) but exhibited the highest displacement (41.46 mm). This suggests that while the absence of stirrups may compromise shear capacity, the beam still experienced significant flexural deformation before failure. Overall, the results emphasize the necessity of a holistic approach in beam design, where concrete strength, reinforcement detailing, and geometric proportions must be carefully balanced to achieve both strength and ductility

Table 24 shows the cracking, yield, and ultimate load capacities of the tested reinforced concrete beams, which further elucidates the influence of concrete compressive strength, reinforcement detailing, and shear span-to-depth (a/d) ratio on structural performance. Beams with higher compressive strength (fc') and well-distributed shear reinforcement demonstrated superior load capacities across all stages of loading. For instance, beam G2B2, with a compressive strength of 57.68 MPa and stirrups spaced at φ6–250 mm, exhibited the highest performance with a cracking load of 39.98 kN, yield load of 295.36 kN, and ultimate load of 302.02 kN. This behavior reflects the positive synergy between concrete strength and transverse reinforcement in delaying cracking and enhancing ductility and load resistance.

Table 24. Load capacity in the crack, yield, and ultimate

Beam	Fc' (MPa)	Reinforcement			a/d	Load Experimental		
		Top	Bot	Stirrups		P Crack (kN)	P Yield (kN)	P Ultimate (kN)
G1A2	51.57	2 ø6	2 D16	ø6 - 200	2	35.04	160.42	208.67
G1B2	58.23	2 ø6	2 D16	ø6 - 250	2	38.05	189.01	230.07
G1B2.5	59.80	2 ø6	2 D16	ø6 - 250	2.5	34.70	141.18	178.01
G2B2	57.68	2 ø6	3 D16	ø6 - 250	2	39.98	295.36	302.02
G1C2	58.19	2 ø6	2 D16	-	2	38.01	125.03	202.36
P1B2	32.59	2 ø6	2 D16	ø6 - 250	2	29.30	130.71	130.71

Conversely, beam P1B2, which had the lowest compressive strength (32.59 MPa), reached the lowest values for cracking (29.30 kN), yield (130.71 kN), and ultimate loads (130.71 kN). The minimal difference between the yield and ultimate loads suggests brittle behavior and limited post-yield capacity. Similarly, beam G1B2.5 with an a/d ratio of 2.5; higher than the others; showed relatively lower performance, emphasizing the detrimental effect of increased shear span on flexural strength and overall load resistance.

Interestingly, beam G1C2, which lacked stirrup reinforcement, still demonstrated relatively high cracking (38.01 kN) and ultimate load (202.36 kN) capacities. However, its lower yield load (125.03 kN) compared to its ultimate load indicates a prolonged inelastic deformation phase, likely due to the absence of confinement, which permitted wider cracking and redistribution of stresses before failure. This observation underscores the importance of stirrup reinforcement in enhancing not only shear resistance but also yielding behavior.

Overall, the experimental data confirm that increasing concrete strength and ensuring adequate stirrup confinement significantly contribute to delaying the onset of cracking, increasing yield thresholds, and achieving higher ultimate capacities. These results validate the critical role of integrated design variables in improving structural integrity under flexural and shear loading conditions.

Figure 14 illustrates the load-deflection behavior of six different beam specimens under mid-span loading. This type of plot is crucial in structural engineering because it reveals how beams respond to applied forces, particularly in terms of strength (peak load capacity), stiffness (initial slope), and ductility (extent of deflection before failure). Each curve corresponds to a different beam type, labeled G1A2, G1B2, G1B2.5, G2B2, P1G2, and G1C2, allowing for comparison of their structural performance.

Among all the specimens, Beam G2B2 (represented by a dotted line) exhibits the highest peak load, reaching approximately 300 kN, which indicates that this beam has the greatest load-bearing capacity. Additionally, the initial slope of this curve is the steepest, suggesting high stiffness—a desirable property in beams that must resist deformation under load. The significant increase in load with minimal deflection initially, followed by a sharp drop, implies that G2B2 is strong but may be more brittle, failing suddenly without much warning.

In contrast, Beam P1G2 and G1A2 show more ductile behavior. Although they do not reach the highest peak loads (both under 225 kN), their curves do not drop off sharply, which suggests gradual failure mechanisms. This kind of behavior is generally preferred in structural applications where deformation prior to failure can provide warning signs, improving safety. The smoother post-peak response indicates these beams can sustain load redistribution even after cracking, likely due to more effective reinforcement or material composition.

Beam G1B2.5 and G1C2 show intermediate behaviors. They achieve relatively high load capacities (around 250–275 kN) but display sudden drops in load, suggesting brittle failures, possibly due to insufficient post-cracking reinforcement or weak concrete-rebar bond. Such behavior can be risky in practical applications where sudden failure without noticeable deflection is undesirable.

Beam G1B2, though reaching a moderate peak load of about 225 kN, demonstrates a steady and controlled response, making it a balance between strength and ductility. The solid line shows a modest decline after the peak, which may indicate cracking followed by some level of load redistribution. This beam may be considered structurally reliable in conditions where both strength and safety margins are necessary. Beam G2B2 stands out for its superior strength and stiffness, making it suitable for applications where load capacity is critical. However, its brittle failure mode could be a disadvantage in terms of structural safety. Beams like P1G2 and G1A2, though weaker, offer better ductility and energy absorption, which are advantageous for seismic or impact-resistant structures. Ultimately, the choice of beam would depend on the design priorities; whether maximum strength, ductility, or a balanced performance is desired.

3.3. Crack Pattern

As G1A2 beam, Figures 14 and 15-a shows that the initial cracking phenomenon is localized within the G1A2 beam's bending region. Experimental findings confirm that the initial crack is observed at a load of 35.04 kN. Furthermore, cracks develop near the support as the applied load gradually increases. Ultimately, beam G1A2 experiences shear failure at a critical load of 208.67 kN. Before the onset of shear failure, the beam undergoes plastic deformation in the compression region directly beneath the loading point. Evidence of compression-induced deformation is also noted in the left support area. This mode of failure can be characterized as shear compression.
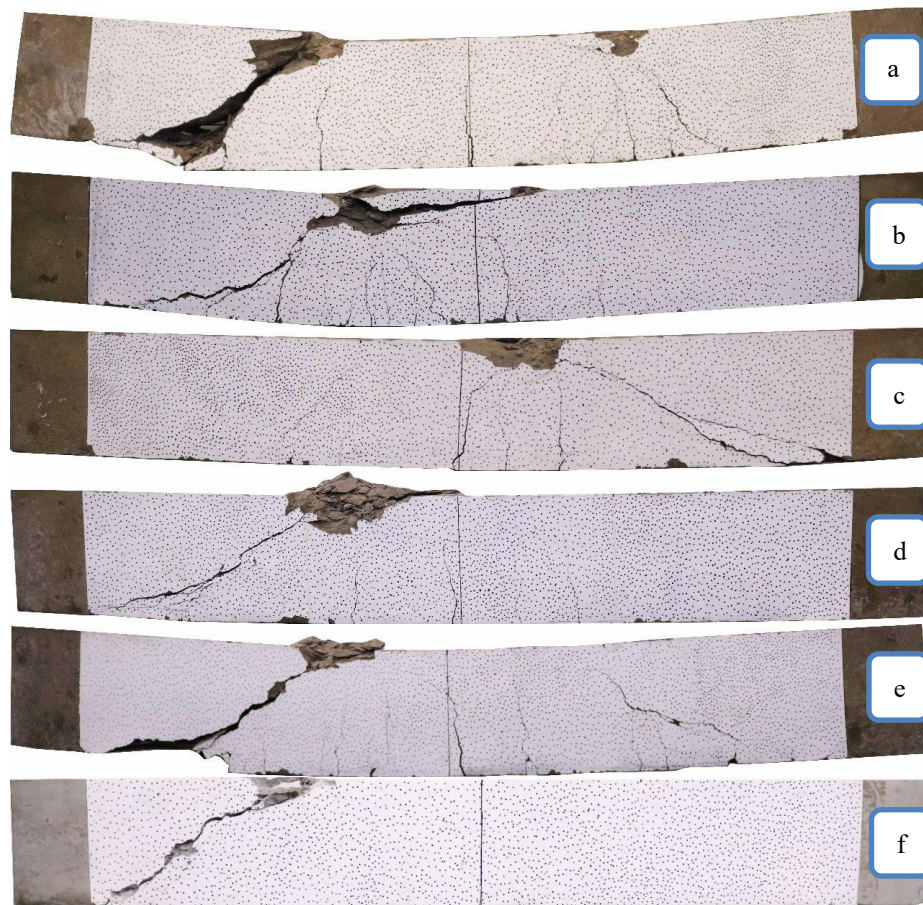

Figure 15. Crack pattern and mode failure of concrete beams; (a) G1A2, (b) G1B2, (c) G1B2.5, (d) G2B2, (e) G1C2, (f) P1B2

In the case of the G1B2 beam type, the initial crack is detected within the bending area at a critical load of 38.05 kN. Subsequently, following the initiation of a flexural crack, it extends towards the support area, ultimately culminating in a shear crack, as illustrated in Figure 15-b. The progressive increment in the applied load leads to shear failure at a peak load of 230.07 kN. Before shear failure occurs, the beam experiences plastic deformation in the compression zone beneath the load location. These patterns of cracks and shear failure are visually depicted in Figure 15(b).

Further detailed observations were conducted on beam G1B2.5, demonstrating its initial crack within the bending area at a critical load of 34.70 kN. Post-crack initiation, the crack propagates toward the support area as Figure 15-c exemplifies. The beam sustains a peak load of 178.01 kN, with plastic deformation observed beneath the loading point before shear failure occurs

As for beam G2B2, it exhibits its initial cracks within the bending area at a critical load of 39.98 kN. Subsequently, these cracks propagate toward the support area as the applied load intensifies. The beam eventually experiences shear failure at a peak load of 302.02 kN. Shear failure becomes evident after the beam undergoes plastic deformation directly beneath the loading point. The progression of cracks and the failure mechanism in beam G2B2 are visually represented in Figure 15-d.

In the case of the G1C2 type beam, as illustrated in Figure 15-e, the first crack emerges within the bending area at a load of 38.01 kN. The crack pattern extends towards the support region as the load applied to the beam increases. Shear failure is observed at a peak load of 202.36 kN, concurrent with plastic deformation occurring at the load placement location in the compression area.

Observations about type P1B2 beams in Figure 15-f indicate a diagonal tension failure mode characterized by brittleness. The initial crack is initiated within the bending area at a load of 29.30 kN. Moreover, as the applied load increases, a diagonal crack widens, eventually transforming into a primary diagonal stress crack on one side, predominantly extending toward the loading point. A brittle failure ultimately occurs at a peak load of 130.71 kN, even before the longitudinal reinforcement yields.

3.3.1. Digital Image Correlation Analysis

To accurately observe and analyze crack patterns on the surface of geopolymer concrete beams during and after loading, the Digital Image Correlation (DIC) method is employed. This non-contact optical technique enables precise measurement of surface deformations and provides valuable insights into crack propagation behavior under applied loads. The concept of this method is to monitor minute deformations by tracking numerous abstract marked points on
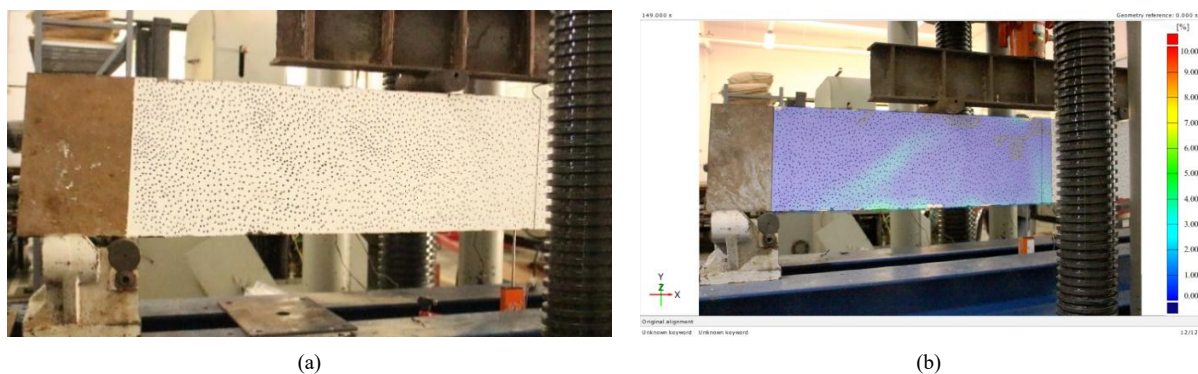

<div align="center">(a)   (b)</div>

Figure 16. (a) Random point marking on the specimen's surface; (b) DIC result in percentage color scale

Various software tools are available for DIC analysis; the open-source software Zeiss Quality Suite is utilized in this study. The process involves marking the surface, positioning cameras perpendicular to it, and ensuring proper alignment. Maintaining this perpendicular angle is critical for accurate scale measurements, as even a slight tilt in the camera's view can significantly affect the analysis results. In this study, due to the large size of the beam samples, the middle section of the beam was obscured by the UTM machine during testing. To address this limitation, two cameras were strategically installed to capture the left and right sides of the beam, as shown in Figure 11-b. These cameras simultaneously capturing images every 1 second, ensuring consistent data collection. The images were then individually processed using Zeiss Quality Suite DIC software to analyze deformation and crack patterns on each beam side.

Figure 17 shows that the Digital Image Correlation (DIC) analysis of experimental beams reveals distinct cracking patterns and failure mechanisms influenced by the shear reinforcement variables. In beam G1A2, shear cracks appeared first with a DIC scale of 2.5%, followed by flexural cracks at mid-span that developed more rapidly, reaching a scale of 7%. Beam G1B2, with a larger stirrup spacing, exhibited more flexural cracks but smaller shear cracks than G1A2. A

similar pattern was observed in G2B2, which had the highest flexural capacity, though shear cracks remained the ultimate failure mode. Beam G1C2, without shear reinforcement, experienced the most flexural cracks, showing a pattern similar to G1A2. In contrast, the PCC concrete beam (P1B2) exhibited only shear cracks, indicating pure shear failure without flexural cracks. These findings highlight the differences in structural behavior between ULCC concrete and PCC and suggest that shear reinforcement ratios have a greater influence on the development of flexural cracks than shear cracks in geopolymer concrete beams. Meanwhile, beam G1B2.5 exhibits the specimens' most distinct shear crack patterns. The shear failure observed is less severe than in other samples, as indicated by the lower intensity in the color scale.
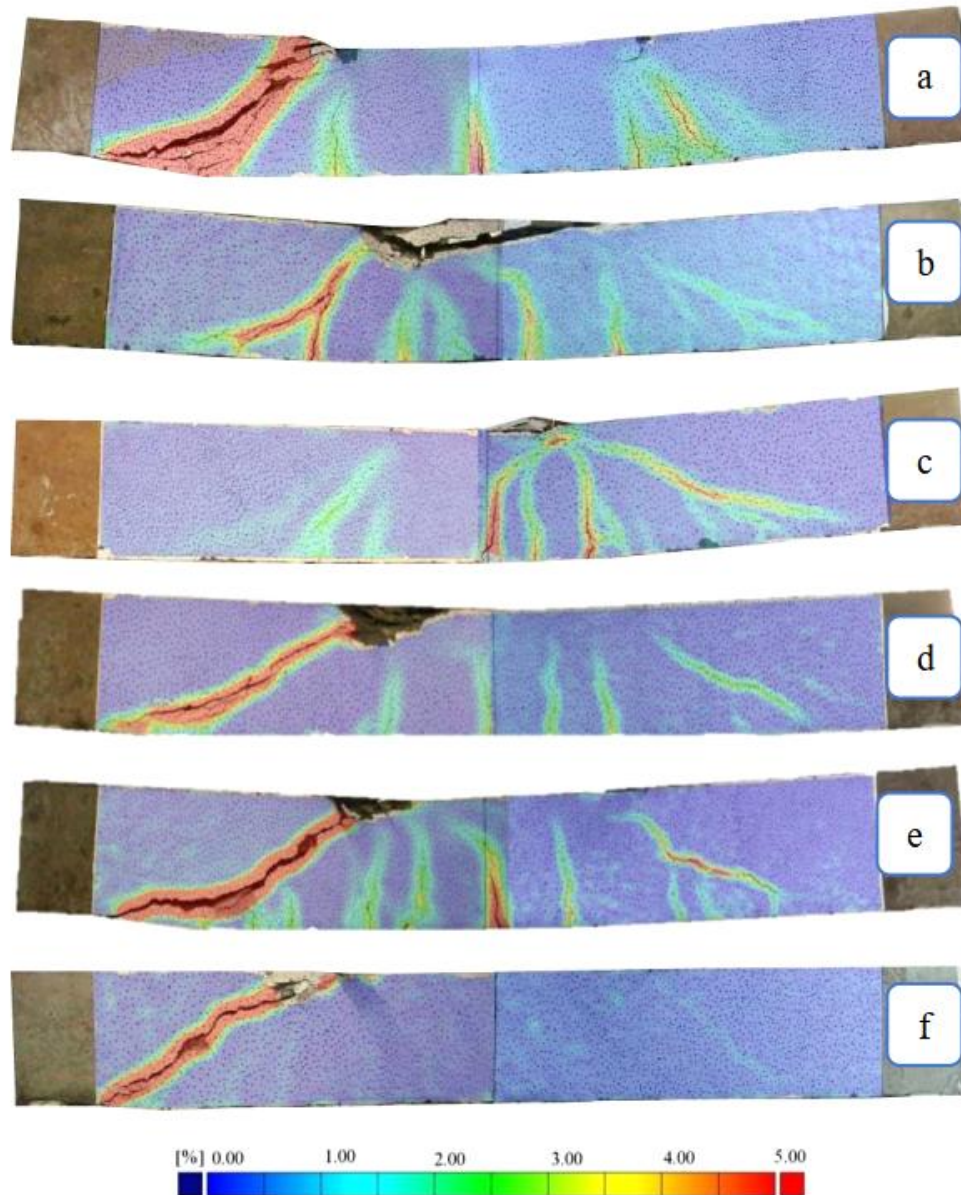

Figure 17. Crack pattern from DIC software of concrete beams; (a) G1A2, (b) G1B2, (c) G1B2.5, (d) G2B2, (e) G1C2, (f) P1B2

3.4. Shear Capacity

The test results of ultra-low carbon concrete (ULCC) and Portland cement concrete (PCC) beams regarding the shear capacity that occurs in each test object are in Table 25. Based on the results shown in Table 25, the shear capacity value in the type G1B2 beam is 115.04 kN. Then, the shear capacity value for type G1A2 beams is 104.34 kN, and the shear capacity value for type G1C2 beams is 101.18 kN. The type G1A2 beam uses stirrup reinforcement at a distance of 200 mm, the type G1B2 beam uses at a distance of 250 mm, and the type G1C2 beam does not use stirrup reinforcement. The shear capacity value of the G1B2 type beam is higher at 10.25% than that of the G1A2 type beam, even though in analytical calculations, the beam with tighter stirrups should have a greater shear capacity. This difference occurs because of differences in concrete compressive strength. The compressive strength quality of the G1A2 beam is 51.57 MPa, while the G1B2 beam is 58.23 MPa.

Table 25. Results of shear capacity values for each test object

| No.	Beam	fc' (MPa)	Reinforcement			a/d	Shear Load
			Top	Bot	Stirrups		Vu Test (kN)
1	G1A2	51.57	2 ø6	2 D16	ø6 - 200	2	104.34
2	G1B2	58.23	2 ø6	2 D16	ø6 - 250	2	115.04
3	G1B2.5	59.80	2 ø6	2 D16	ø6 - 250	2.5	89.00
4	G2B2	57.68	2 ø6	3 D16	ø6 - 250	2	151.01
5	G1C2	58.19	2 ø6	2 D16	-	2	101.18
6	P1B2	32.59	2 ø6	2 D16	ø6 - 250	2	65.35

Meanwhile, comparing the G1B2 type beam to the G1C2 type beam, the shear capacity value decreased by 12.05%. Therefore, the installation of shear reinforcement affects increasing the shear capacity. Research also stated by Piscesa et al. [49] that the increase in shear reinforcement is directly proportional to the increase in shear force in reinforced concrete beams.

Furthermore, beams of type G1B2 and G1B2.5 have different values for shear capacity based on test results, as shown in Figure 17. The G1B2 type beam has a shear capacity value of 22.63% higher than the G1B2.5 type beam. The shear capacity in the G1B2 type beam is 115.04 kN, and the G1B2.5 type beam has a value of 89.00 kN. This difference occurs because there are differences in the location of the loading a/d. The value a/d 2 has a greater capacity than the load location value a/d 2.5 analytical calculations; the beam with tighter stirrups should have a greater shear capacity. This difference occurs because there are differences in concrete compressive strength. The compressive strength quality of the G1A2 beam is 51.57 MPa, while the G1B2 beam is 58.23 MPa

Apart from discussing the influence of shear reinforcement and the influence of a/d loading location, the variable that is also addressed in this research is the influence of longitudinal reinforcement on the shear capacity that occurs in geopolymer-reinforced concrete beams. The results of the shear capacity values contained in Table 25 show that the G2B2 beam has a shear capacity value that is 31.27% greater than the G1B2 type beam with a value of 151.01 kN respectively for the G2B2 beam type, and the G1B2 type beam has a value of 115.04 kN. The difference in the amount of flexural reinforcement in the G2B2 beam, which is more than the G1B2 type beam, causes an increase in the beam's capacity. Apart from the variables above, the differences in the shear capacity of ultra-low carbon concrete (ULCC) and Portland cement concrete (PCC) beams are also discussed. The P1B2 type beam is a Portland cement concrete (PCC) beam whose shear capacity value is lower than the G1B2 type beam. The capacity value that occurs in the P1B2 beam is 65.35 kN, while the G1B2 type beam has a shear capacity value of 115.04 kN. However, this cannot be used as a comparison reference because the concrete quality values in the G1B2 and P1B2 blocks have significant differences. The G1B2 beam has a value of 58.23 MPa, while the quality for the P1B2 beam is 32.6 MPa.

3.5. Load Strain Behavior

The load-strain curves that occur in the flexural reinforcement and shear reinforcement during the two-point load test are in Figures 18 to 22. Flexural reinforcement strains that appear at the midpoint of the beam span and the shear reinforcement strains are measured at the midpoint of the shear reinforcement leg. Measurement of the strain of flexural reinforcement and shear reinforcement using a strain gauge. The location of the strain gauge placement on each test specimen is in Figure 6.
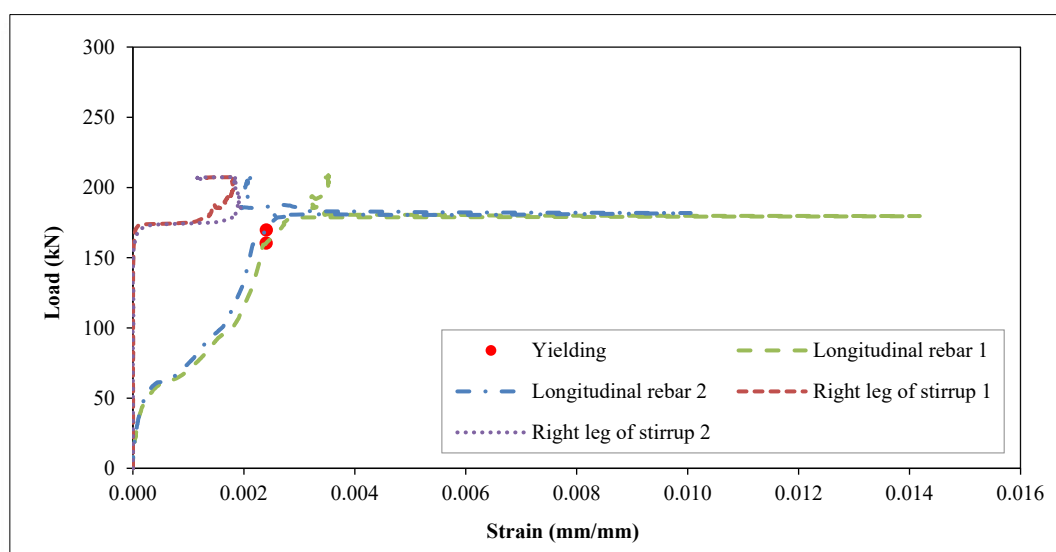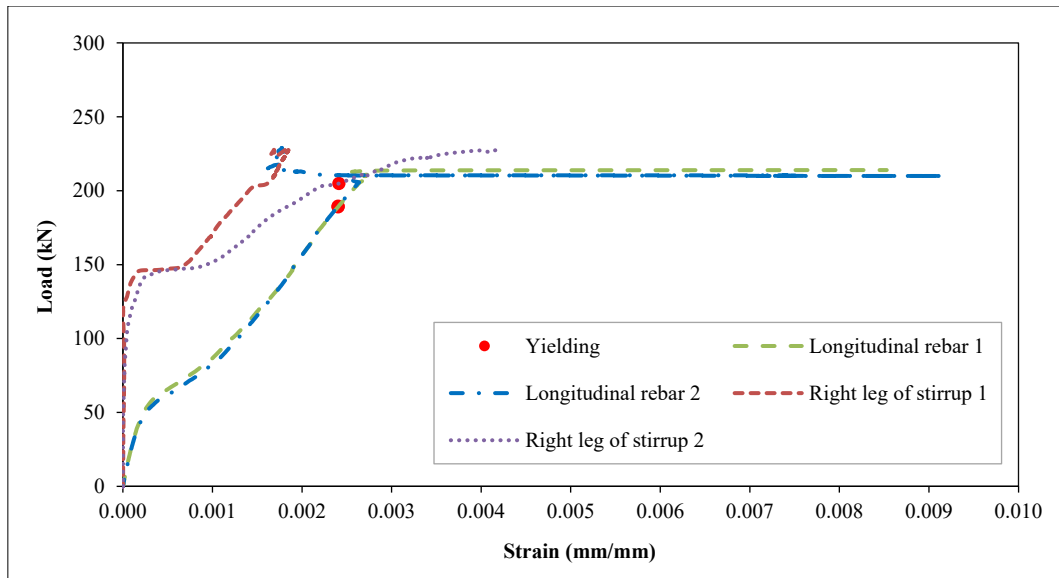

Figure 18. Load-strain beam type G1A2

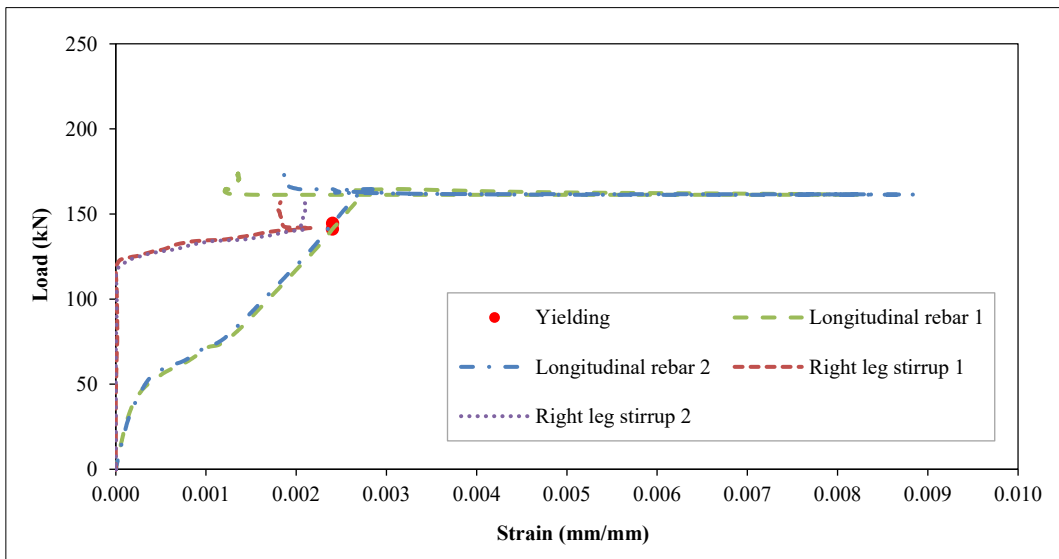**Figure 19. Load-strain beam type G1B2**

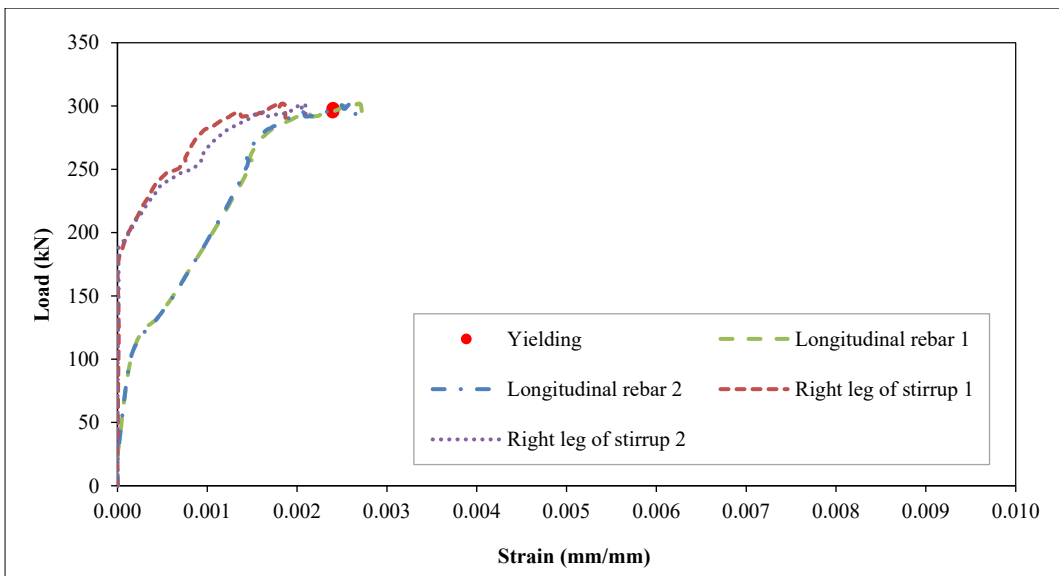**Figure 20. Load-strain beam type G1B2.5**

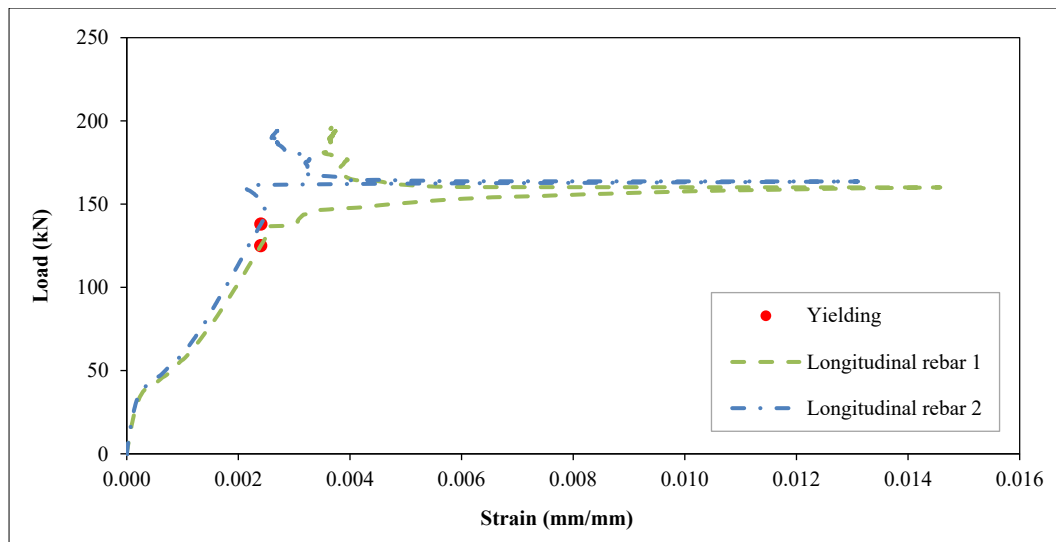**Figure 21. Load-strain beam type G2B2**

Figure 22. Load-strain beam type G1C2

The yield strain in the flexural reinforcement calculated from $\varepsilon = fy/Es$, $\varepsilon=477.33/200000$ is 2.4×10^{-3} mm/mm, and for the yield strain in the shear reinforcement, it is $\varepsilon=476.67/200000 = 2.4 \times 10^{-3}$ mm/mm. The fy and fu steel qualities of each reinforcement from the material test results are in Table 13. The maximum strain of flexural reinforcement in type G1A2 beams exceeds the yield point at 14.2×10^{-3} mm/mm. Meanwhile, the maximum strain of the shear reinforcement on the right side of this beam is 2.0×10^{-3} mm/mm, so the shear reinforcement has not yielded. The load strain curve for the G1A2 type beam is in Figure 18.

Figure 19 shows the flexural and shear reinforcement load-strain curves in the G1B2-type beam. The measurements using a strain gauge show that the maximum strain of the flexural reinforcement at the middle of the span is 9.2×10^{-3} mm/mm, exceeding the yield strain of 2.4×10^{-3} mm/mm. Furthermore, the maximum strain of the shear reinforcement also exceeds the yield strain with a value of 4.2×10^{-3} mm/mm.

The results of strain measurements for the flexural reinforcement and shear reinforcement of the G1B2.5 type beam are in Figure 20. The maximum strain in the flexural reinforcement is 8.8×10^{-3} mm/mm, while the shear reinforcement on the right side of the beam is 2.2×10^{-3} mm/mm. It shows that the longitudinal reinforcement yielded, while the shear reinforcement did not. Apart from that, the measurement of type G2B2 beam results in Figure 21 shows that the maximum strains in bending and shear reinforcement are 7.1×10^{-3} mm/mm and 2.1×10^{-3} mm/mm, respectively. Longitudinal reinforcement on the type G2B2 beam yielded, while shear reinforcement did not.

Figure 23 shows the load-strain curve on a type P1B2 beam while Figure 22 shows the results of strain measurements presented as a load-strain curve for a type G1C2 beam. The maximum strain measurement results of the bending reinforcement for beams of type P1B2 and G1C2 were 2.0×10^{-3} mm/mm and 14.6×10^{-3} mm/mm, respectively. It shows that the flexural reinforcement in the P1B2 beam does not yield, and the flexural reinforcement in the G1C2 beam yields. Furthermore, the shear reinforcement in the P1B2 type beam has a strain of 0.3×10^{-3} mm/mm, and the shear reinforcement does not yield as well as longitudinal reinforcement. Meanwhile, in the G1C2 type beam, there is no shear reinforcement.
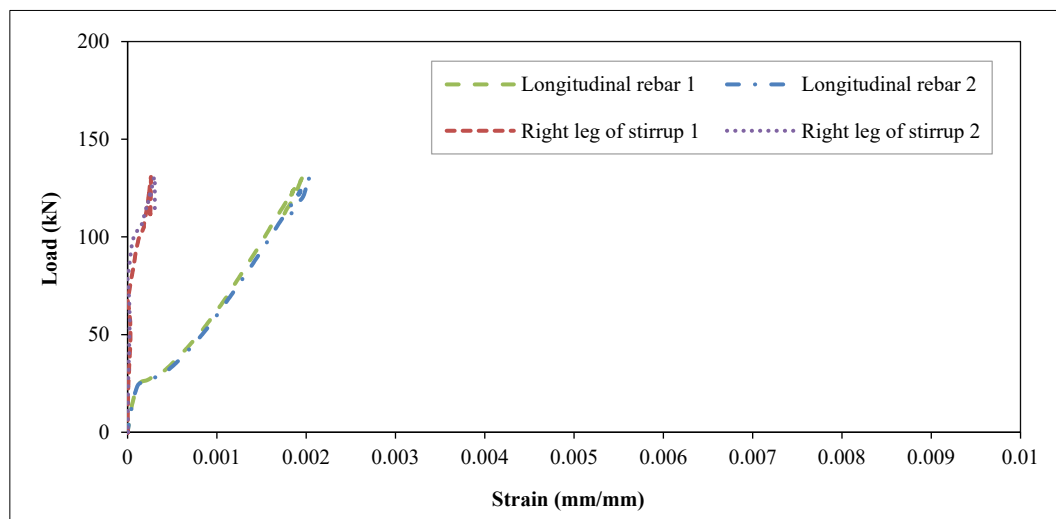

Figure 23. Load-strain beam type P1B2

3.6. Comparison of Shear Capacity with ACI 318-19

The comparison is based on Table 26 shows that the shear capacity ratio for type G1A2 beams has a Vu Test/Vn ACI-19 value of 1.65. Then, for the shear capacity of beams G1B2, G1B2.5, G2B2, and G1C2, the Vu Test/ Vn ACI-19 values are 1.91, 1.46, 2.32, and 2.60. Meanwhile, the comparison value for Portland cement concrete beams (PCC) with the P1B2 beam type, the Vu Test/ Vn ACI-19 value, is 1.29.

Table 26. Comparison shear capacity experimental vs ACI 318-19

Beam	Fc' (MPa)	Reinforcement			a/d	Shear Load		
		Top	Bot	Stirrups		Vu Test (kN)	Vn ACI 318-19 (kN)	Vu Test/ Vn ACI 318-19
G1A2	51.57	2 ø6	2 D16	ø6 - 200	2	104.34	63.36	1.65
G1B2	58.23	2 ø6	2 D16	ø6 - 250	2	115.04	60.29	1.91
G1B2.5	59.80	2 ø6	2 D16	ø6 - 250	2.5	89.00	60.81	1.46
G2B2	57.68	2 ø6	3 D16	ø6 - 250	2	151.01	65.14	2.32
G1C2	58.19	2 ø6	2 D16	-	2	101.18	38.85	2.60
P1B2	32.59	2 ø6	2 D16	ø6 - 250	2	65.35	50.50	1.29
						Mean		1.87
						COV (%)		24.75

Table 26 presents a comparative analysis between the experimental shear capacity (Vu Test) of geopolymer concrete beams and the predicted nominal shear strength (Vn) calculated based on ACI 318-19 provisions. The ratio of experimental to predicted values (Vu Test / Vn ACI 318-19) provides insight into how well the ACI code estimates shear capacity for this type of material. Across all six beam specimens, the experimental values exceed the ACI predictions, with ratios ranging from 1.29 (P1B2) to 2.60 (G1C2), indicating that the actual performance of the geopolymer concrete beams is significantly higher than what is anticipated by conventional code-based models. The highest discrepancy is observed in beam G1C2, which lacked shear reinforcement (stirrups), yet showed a high test-to-code ratio, suggesting that the contribution of the matrix and aggregate interlock in geopolymer concrete may be underestimated by ACI 318-19. Conversely, the lowest ratio was seen in P1B2, which also had the lowest compressive strength. The average ratio across all specimens is 1.87, with a coefficient of variation (COV) of 24.75%, indicating notable variability in the accuracy of ACI predictions for geopolymer concrete. Overall, the results suggest that ACI 318-19 underestimates the shear capacity of geopolymer concrete beams, highlighting the need for further research and potential adjustments to code provisions when applied to alternative cementitious materials.

3.7. Comparison of Test Results with Analytical Calculations

Table 27 shows the average value of comparing the load when the crack occurs from the experimental results with the results of the analytical calculation P Crack Exp./ P Crack Calc. of 0.97 with a COV value of 4%. Then, the average comparison value when the lower bending reinforcement experiences yield results from experiments with analytical calculations P Yield Exp./ P Yield Calc. of 0.94 with a COV value of 16.90%. Meanwhile, the average value compares the peak load from the experimental results with the analytical calculation of the peak load when the concrete strain is 0.003 mm/mm is P ultimate Exp/P ultimate Calc. of 1.10 with a COV value of 15.03%.

Table 27. Comparison load experimental vs. analytical calculation

Beam	Load Experimental			Load Calculation			Experimental/ Calculation		
	P Crack (kN)	P Yield (kN)	P Ultimate (kN)	P Crack (kN)	P Yield (kN)	P Ultimate (kN)	P Crack Exp./ Calc.	P Yield Exp./ Calc.	P Ulti. Exp./ Calc.
G1A2	35.04	160.42	208.67	37.59	173.10	180.59	0.93	0.93	1.16
G1B2	38.05	189.01	230.07	39.76	173.59	181.83	0.96	1.09	1.27
G1B2.5	34.70	141.18	178.01	32.93	142.08	148.98	1.05	0.99	1.19
G2B2	39.98	295.36	302.02	40.44	255.31	265.34	0.99	1.16	1.14
G1C2	38.01	125.03	202.36	39.74	173.55	181.82	0.96	0.72	1.11
P1B2	29.30	130.71	130.71	30.50	174.68	174.68	0.96	0.76	0.75
						Mean	0.97	0.94	1.10
						COV (%)	4.00	16.90	15.03

Table 27 provides a comparison between experimental results and analytical calculations for cracking, yielding, and ultimate loads in geopolymer concrete beams. The table is divided into three sections: the first reports the experimental loads at cracking (P Crack), yielding (P Yield), and ultimate failure (P Ultimate); the second provides the corresponding values obtained from analytical predictions; and the third presents the ratios of experimental to calculated values for each load stage. Overall, the experimental cracking loads are slightly lower than the calculated ones, with an average ratio of 0.97 and a low coefficient of variation (COV) of 4.00%, indicating consistent agreement. For yielding loads, the average ratio is 1.06 with a higher variability (COV of 16.90%), suggesting that experimental results generally exceed predictions but with less consistency. The ultimate load comparison shows the highest deviation, with experimental loads surpassing analytical values by an average ratio of 1.10 and a COV of 15.03%. Notably, beam P1B2 exhibits the lowest ultimate load ratio (0.75), indicating a significant underperformance compared to predictions, potentially due to its lower compressive strength. These findings highlight that while analytical models provide reasonably accurate estimates for initial cracking behavior, they tend to underestimate the yield and ultimate capacities of geopolymer concrete beams. This suggests a conservative bias in traditional calculation methods when applied to non-conventional materials and reinforces the need for tailored models or modification factors for improved prediction accuracy in geopolymer systems.

3.8. Comparison of Load-Deflection Curve Experimental Results with Finite Element Analysis

Figures 24 to 29 present the load-deflection curves for reinforced geopolymer concrete (GPC) beams and conventional concrete (PCC) beams, developed using 3D Nonlinear Finite Element Analysis (3D-NLFEA). The study evaluates the peak load and deflection of five reinforced GPC beams and one PCC beam, comparing the results obtained from the 3D-NLFEA simulations with experimental data.
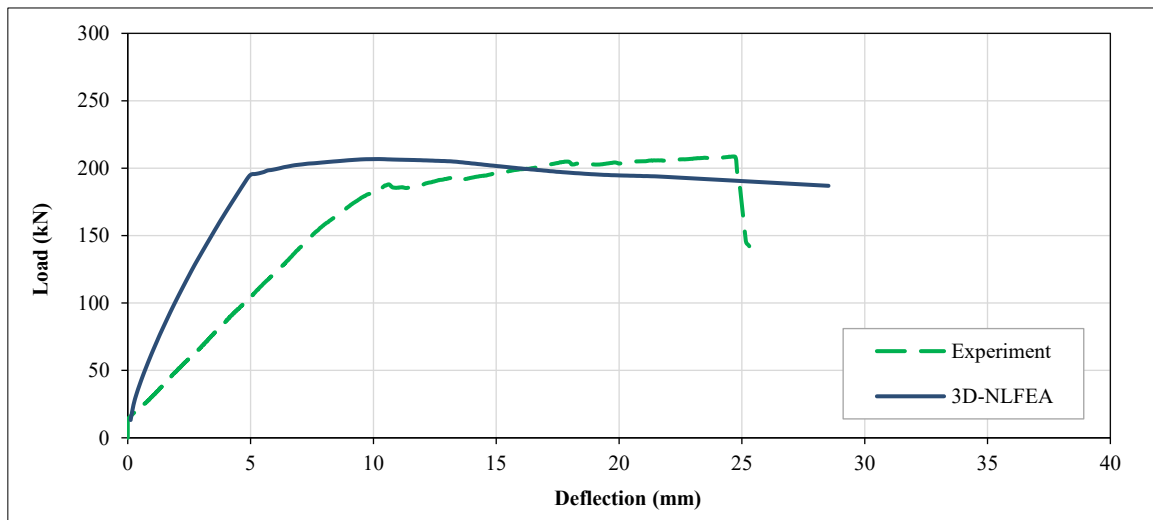

Figure 24. Comparison of peak load-deflection curves obtained from 3D Nonlinear Finite Element Analysis (3D-NLFEA) and experimental data for the G1A2 beam type

Figure 25. Comparison of peak load-deflection curves obtained from 3D Nonlinear Finite Element Analysis (3D-NLFEA) and experimental data for the G1B2 beam type

Figure 26. Comparison of peak load-deflection curves obtained from 3D Nonlinear Finite Element Analysis (3D-NLFEA) and experimental data for the G1B2.5 beam type

Figure 27. Comparison of peak load-deflection curves obtained from 3D Nonlinear Finite Element Analysis (3D-NLFEA) and experimental data for the G2B2 beam type

Figure 28. Comparison of peak load-deflection curves obtained from 3D Nonlinear Finite Element Analysis (3D-NLFEA) and experimental data for the G1C2 beam type
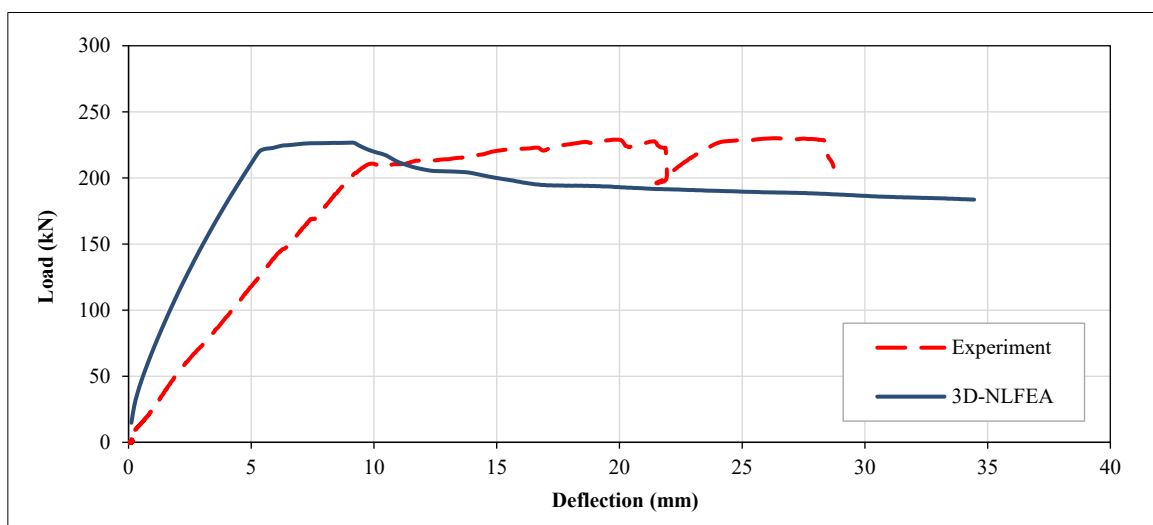
Figure 29. Comparison of peak load-deflection curves obtained from 3D Nonlinear Finite Element Analysis (3D-NLFEA) and experimental data for the P1B2 beam type
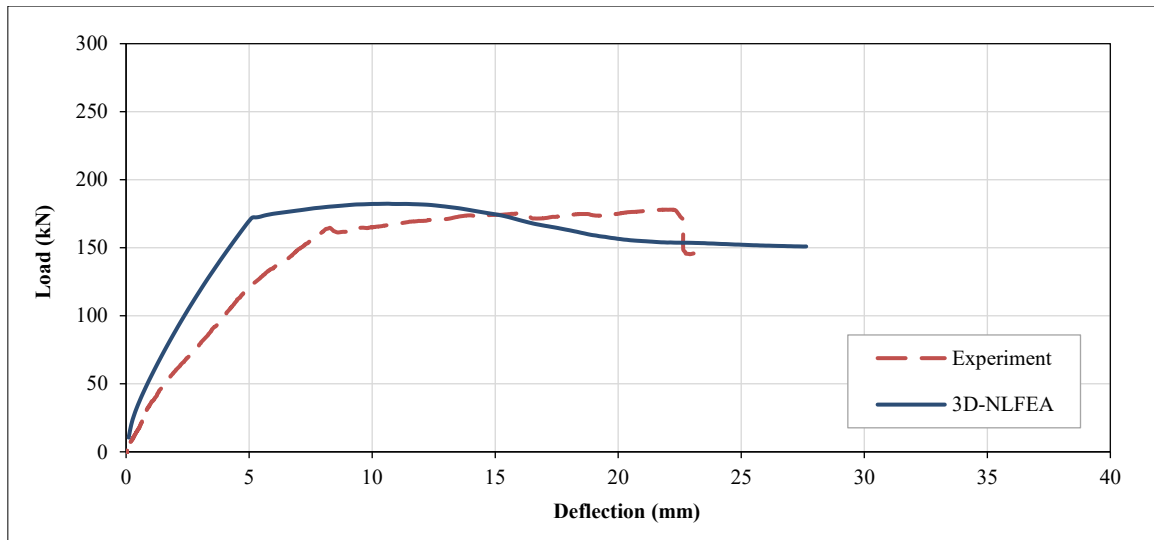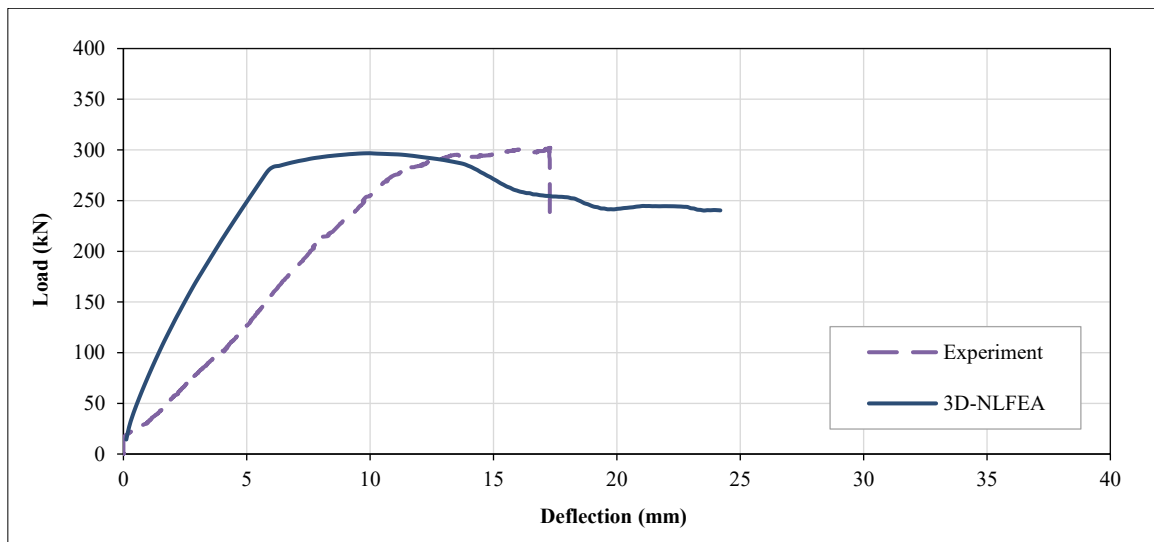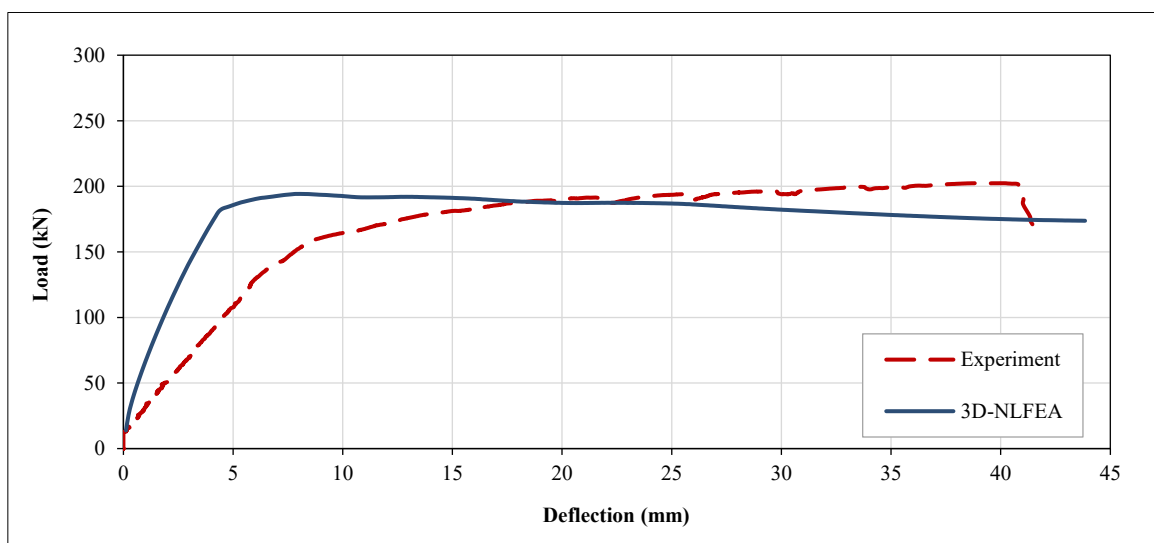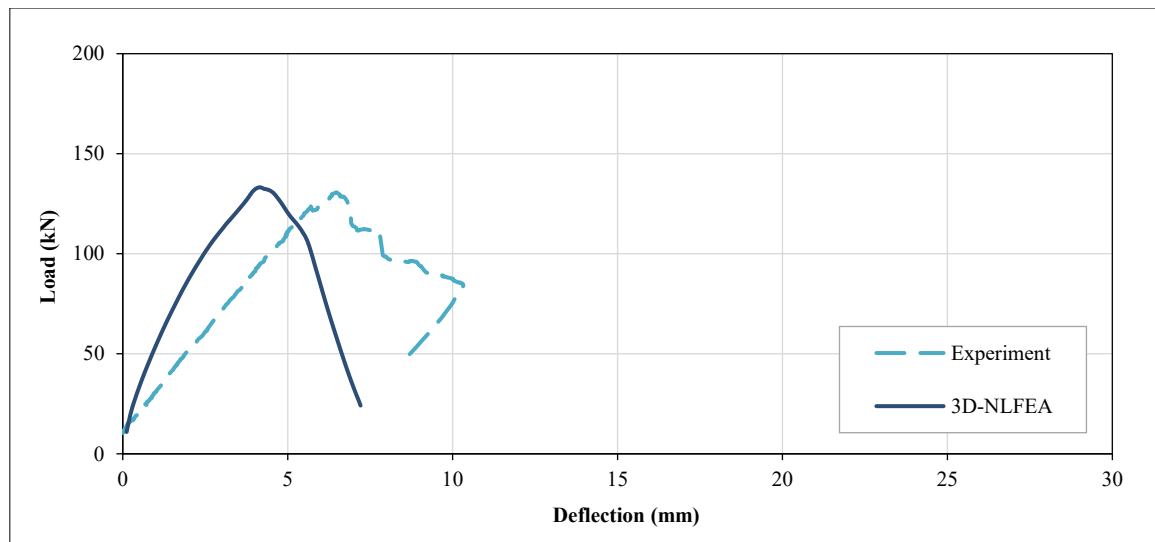
The load-deflection curve comparison for the G1A2 beam type, shown in Figure 24, demonstrates negligible differences between the experimental and simulated results. The 3D-NLFEA simulation predicts a peak load of 206.77 kN, while the experimental test records 208.67 kN, yielding a Pu test/Pu 3D-NLFEA ratio of 1.01. This ratio indicates a slight overestimation of the experimental peak load by the 3D-NLFEA. The detailed results, including peak load values and their ratios, are summarized in Table 28.

Table 28. The comparison of load at cracking, load at yielding, and peak load between experimental results and 3D-NLFEA modeling results

Beam	Load Experimental			3D-NLFEA			Experimental/ Calculation		
	P Crack (kN)	P Yield (kN)	P Ultimate (kN)	P Crack (kN)	P Yield (kN)	P Ultimate (kN)	P Crack Exp./ Calc.	P Yield Exp./ Calc.	P Ulti. Exp./ Calc.
G1A2	35.04	160.42	208.67	38.98	193.26	206.77	0.90	0.83	1.01
G1B2	38.05	189.01	230.07	43.98	214.90	226.68	0.87	0.88	1.01
G1B2.5	34.70	141.18	178.01	31.89	165.32	182.38	1.09	0.85	0.98
G2B2	39.98	295.36	302.02	44.73	280.50	296.71	0.89	1.05	1.02
G1C2	38.01	125.03	202.36	40.93	174.08	193.92	0.93	0.72	1.04
P1B2	29.30	130.71	130.71	32.36	133.20	133.20	0.91	0.98	0.98
						Mean	0.93	0.89	1.01
						COV (%)	7.81	12.13	2.27

Figure 25 illustrates the comparison of the load-deflection curve for the G1B2 beam type. The peak load obtained from the 3D-NLFEA modeling is 226.68 kN, while the experimental peak load is 230.07 kN. Consequently, as presented in Table 28, the ratio of the experimental peak load to the 3D-NLFEA modeled peak load, Pu test/ Pu 3D-NLFEA, is calculated to be 1.01.

Based on Table 28, the ratio of the experimental peak load to the 3D-NLFEA modeled peak load for the G1B2.5 beam type is Putest/Pu3D−NLFEA = 0.98. This ratio is derived from comparing the experimental peak load of 178.01 kN and the 3D-NLFEA modeled peak load of 182.38 kN. The load-deflection curve comparing the 3D-NLFEA modeled peak load with the experimental peak load for the G1B2.5 beam is shown in Figure 26.

Figure 27 shows the comparison of load-deflection curves between the experimental results and the 3D-NLFEA modeling for the G2B2 beam type. According to Figure 27, the experimental peak load is 302.02 kN, while the 3D-NLFEA modeled peak load is 296.71 kN. The ratio of Putest/Pu3D−NLFEA, as listed in Table 28, is 1.02.

The comparison of load-deflection curves for the G1C2 beam type, as shown in Figure 28, indicates an experimental peak load of 202.36 kN and a 3D-NLFEA modeled peak load of 193.92 kN. Consequently, the ratio of Pu test/Pu 3D−NLFEA, as presented in Table 28, is 1.04.

For the P1B2 beam type, the peak load obtained from 3D-NLFEA modeling is 133.20 kN, while the experimental peak load is 130.71 kN. Thus, the ratio of Pu test/Pu 3D−NLFEA is 0.98. The load-deflection curve comparison for the P1B2 beam is shown in Figure 29, and the peak load comparison is presented in Table 28.

3.9. Comparison of Experimental Load Results with Finite Element Analysis

This section compares the experimental and finite element modeling results for the load at cracking, the yielding of the tensile reinforcement, and the peak load. The finite element modeling was conducted using the 3D-NLFEA software. This comparison aims to evaluate the differences in the behavior of ULCC and Portland cement concrete (PCC) beams at the cracking load, yielding load, and peak load, as determined through experimental testing and 3D-NLFEA modelling.

As shown in Table 28, the average ratio of P Crack Exp./P Crack 3D-NLFEA is 0.93, with a coefficient of variation (COV) of 7.81%. At the yielding condition, where the bottom flexural reinforcement yields at a strain of 0.0024 mm/mm, the average ratio of P Yield Exp./P Yield 3D-NLFEA is 0.89, with a COV of 12.13%. For the comparison at peak load, the average ratio of P Ultimate Exp./P Ultimate 3D-NLFEA is 1.01, with a COV of 2.27%.

3.10. Comparison of Crack Patterns Derived from DIC and FEM Analyses

The comparison of crack patterns discussed in this subsection involves analyzing the patterns obtained through Digital Image Correlation (DIC) analysis and those derived from finite element modeling using 3D-NLFEA software. The crack patterns from DIC analysis and 3D-NLFEA modeling are compared under three conditions: when the beam first exhibits cracking, under yield load conditions, and at the peak load state. The strain in the bottom flexural reinforcement under peak load conditions is also compared.

Based on Figure 30, it can be observed that the crack pattern of the G1A2 beam type at the initial cracking stage corresponds to an experimental load of 35.04 kN with a reinforcement strain of 0.000 mm/mm. In the 3D-NLFEA model, cracking occurs under the same load of 35.04 kN with an identical reinforcement strain of 0.000 mm/mm. The observed cracks in the experimental results and the 3D-NLFEA simulation are in the flexural region. At a load of 160.42 kN, the bottom flexural reinforcement in the experimental results yields a strain of 0.0024 mm/mm. Under the same load in the 3D-NLFEA model, the flexural reinforcement strain is 0.0018 mm/mm. The crack pattern observed at this stage includes both shear and flexural cracks. At the ultimate load condition, the experimental results indicate a peak load of 208.67 kN with a reinforcement strain of 0.0142 mm/mm, whereas the 3D-NLFEA simulation shows a peak load of 206.77 kN with a reinforcement strain of 0.0114 mm/mm.
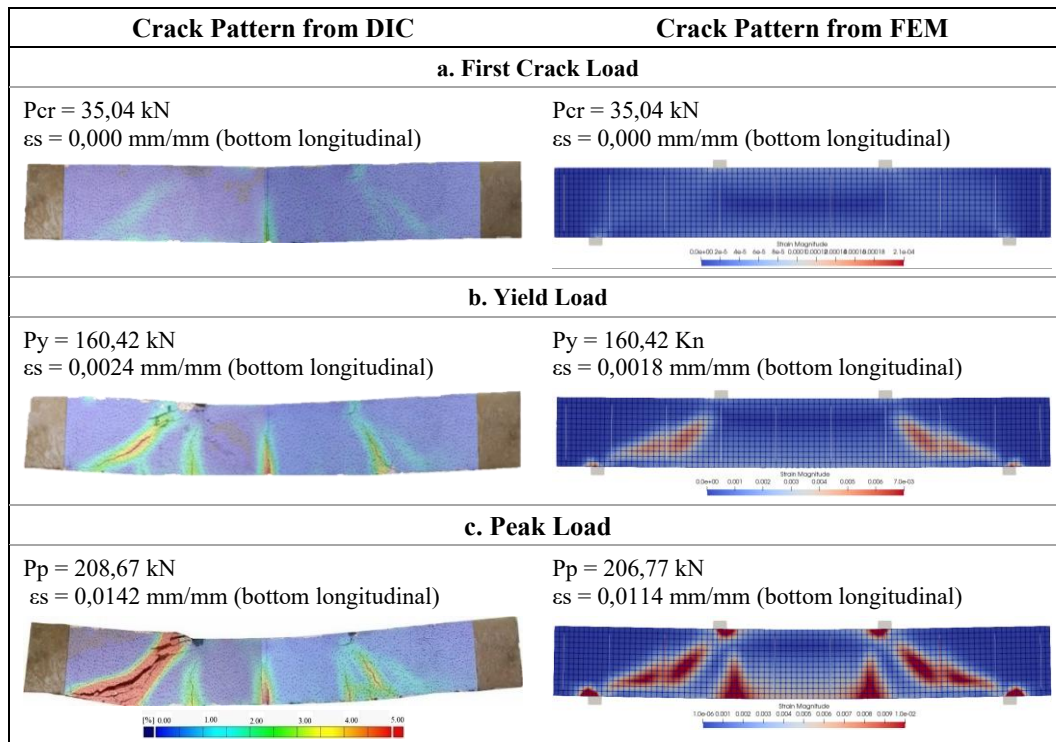
Crack Pattern from DIC	Crack Pattern from FEM
a. First Crack Load	
Pcr = 35,04 kN εs = 0,000 mm/mm (bottom longitudinal)	Pcr = 35,04 kN εs = 0,000 mm/mm (bottom longitudinal)
b. Yield Load	
Py = 160,42 kN εs = 0,0024 mm/mm (bottom longitudinal)	Py = 160,42 Kn εs = 0,0018 mm/mm (bottom longitudinal)
c. Peak Load	
Pp = 208,67 kN εs = 0,0142 mm/mm (bottom longitudinal)	Pp = 206,77 kN εs = 0,0114 mm/mm (bottom longitudinal)

Figure 30. Comparison of crack patterns from DIC analysis and FEM for the G1A2 beam type

Figure 31 presents the crack patterns for the G1B2 beam type as analyzed using DIC and modeled with 3D-NLFEA under three conditions: at an initial cracking load of 38.05 kN, at a load of 189.01 kN, and at a peak load. Both experimental and 3D-NLFEA results indicate cracking occurs at 38.05 kN with a bottom flexural reinforcement strain of 0.000 mm/mm. At 189.01 kN, the experimental data show reinforcement yielding with a strain of 0.0024 mm/mm, while the 3D-NLFEA model predicts a slightly lower strain of 0.0021 mm/mm without yielding. At the peak load, the experiment recorded 230.07 kN with a strain of 0.0092 mm/mm, compared to 226.68 kN and 0.0087 mm/mm in the 3D-NLFEA simulation. The observed failure mode for the G1B2 beam is shear compression failure.
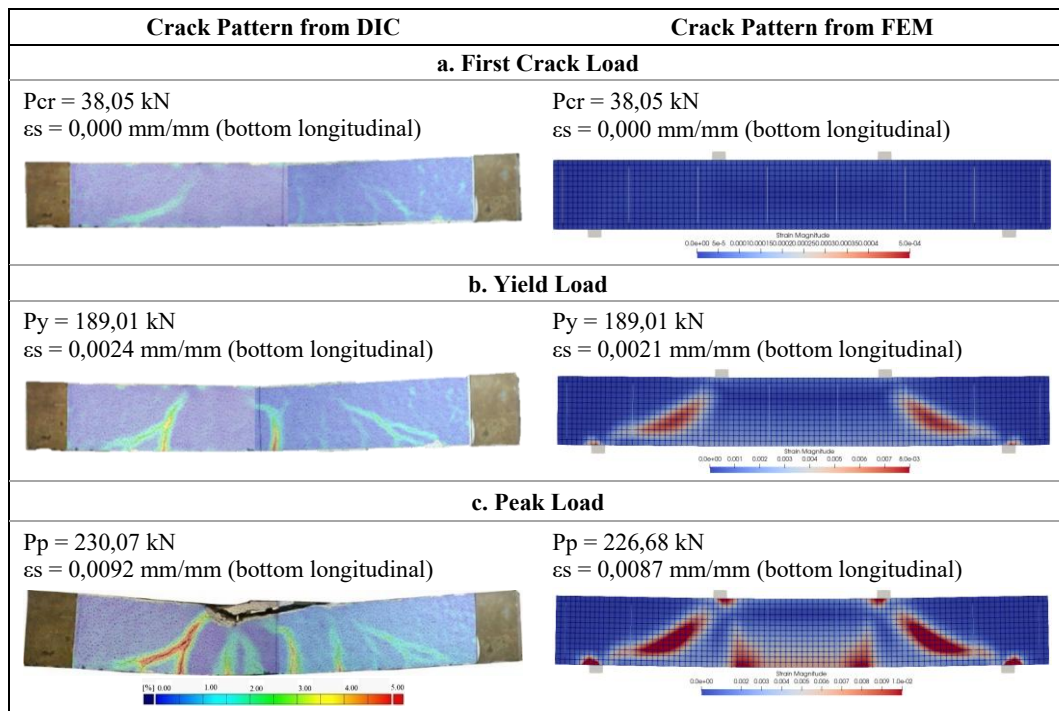
Crack Pattern from DIC	Crack Pattern from FEM
a. First Crack Load	
Pcr = 38,05 kN εs = 0,000 mm/mm (bottom longitudinal)	Pcr = 38,05 kN εs = 0,000 mm/mm (bottom longitudinal)
b. Yield Load	
Py = 189,01 kN εs = 0,0024 mm/mm (bottom longitudinal)	Py = 189,01 kN εs = 0,0021 mm/mm (bottom longitudinal)
c. Peak Load	
Pp = 230,07 kN εs = 0,0092 mm/mm (bottom longitudinal)	Pp = 226,68 kN εs = 0,0087 mm/mm (bottom longitudinal)

Figure 31. Comparison of crack patterns from DIC analysis and FEM for the G1B2 beam type

Figure 32 highlights the performance of the G1B2.5 beam type under various loading conditions. At an initial cracking load of 34.70 kN, experimental results indicate cracking, whereas the 3D-NLFEA model shows no cracking under the same load, with both approaches reporting a strain of 0.000 mm/mm. At 141.18 kN, the bottom flexural reinforcement in the experimental results yields a strain of 0.0024 mm/mm, while the 3D-NLFEA model predicts a strain of 0.0019 mm/mm, indicating no yielding. At peak load, the experimental analysis records a load of 178.01 kN and a strain of 0.0088 mm/mm, compared to 182.38 kN and 0.0102 mm/mm in the 3D-NLFEA model. Crack patterns during initial cracking reveal flexural and shear cracks in the experiment, while the 3D-NLFEA model indicates only flexural cracks. As the load increases toward the yielding condition, shear cracks develop in both cases. At the peak load, experimental and 3D-NLFEA results exhibit crack patterns consistent with shear compression failure.
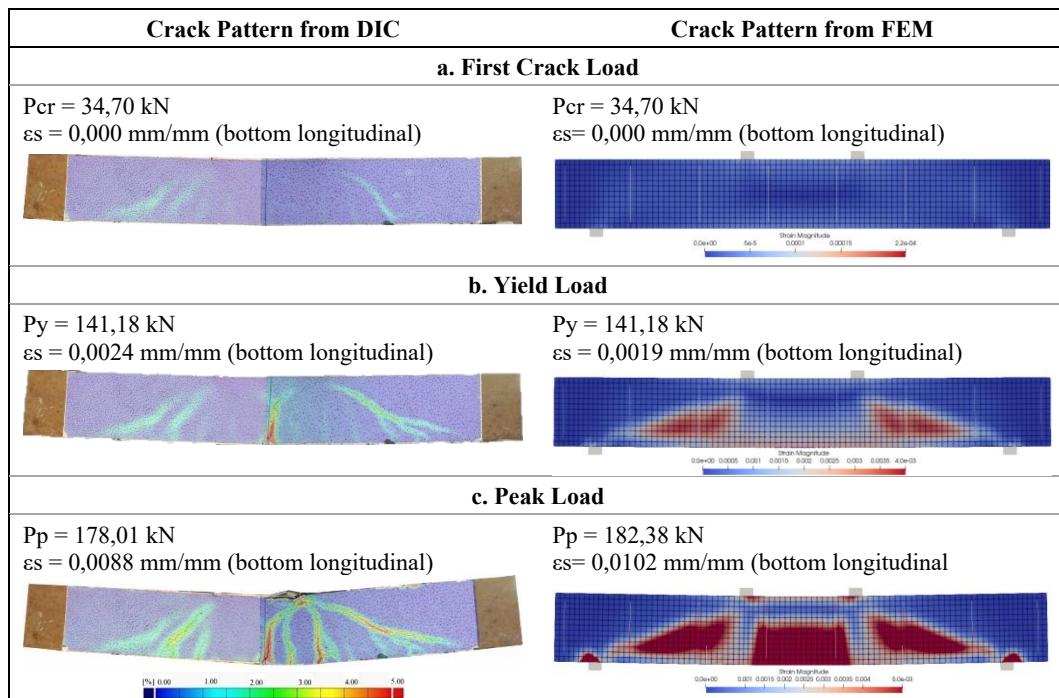
Crack Pattern from DIC	Crack Pattern from FEM
a. First Crack Load	
Pcr = 34,70 kN εs = 0,000 mm/mm (bottom longitudinal)	Pcr = 34,70 kN εs= 0,000 mm/mm (bottom longitudinal)
b. Yield Load	
Py = 141,18 kN εs = 0,0024 mm/mm (bottom longitudinal)	Py = 141,18 kN εs = 0,0019 mm/mm (bottom longitudinal)
c. Peak Load	
Pp = 178,01 kN εs = 0,0088 mm/mm (bottom longitudinal)	Pp = 182,38 kN εs= 0,0102 mm/mm (bottom longitudinal

Figure 32. Comparison of crack patterns from DIC analysis and FEM for the G1B2.5 beam type

Figure 33 compares the crack patterns of the G2B2 beam type obtained from DIC analysis and finite element modeling using 3D-NLFEA software. The experimental results show that cracking occurs at a load of 39.98 kN with a reinforcement strain of 0.000 mm/mm, while under the same load, the 3D-NLFEA model predicts no cracking with a strain of 0.000 mm/mm. The initial crack in the experiment is identified as a shear crack, whereas the 3D-NLFEA model

shows a flexural crack. At a load of 295.36 kN, corresponding to a reinforcement strain of 0.0024 mm/mm in the experiment, flexural and shear cracks are observed, while the 3D-NLFEA model at the same load predicts a bottom reinforcement strain of 0.0025 mm/mm. At peak load, both experimental and 3D-NLFEA results reveal shear compression failure as the failure mode, occurring at 302.02 kN in the experiment and 296.71 kN in the 3D-NLFEA model. The strains at peak load are recorded as 0.0027 mm/mm experimentally and 0.0088 mm/mm in the 3D-NLFEA simulation.
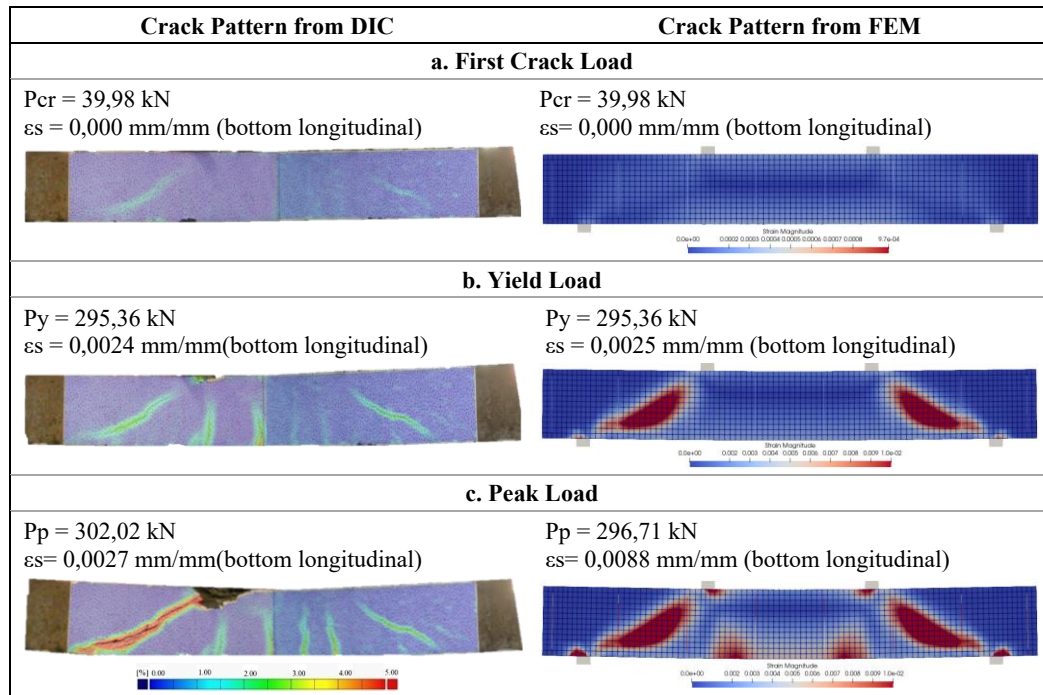

Figure 33. Comparison of crack patterns from DIC analysis and FEM for the G1B2.5 beam type

Figure 34 illustrates the crack patterns of the G1C2 beam type as analyzed through DIC and simulated using 3D-NLFEA under three conditions: at the cracking load, the yielding load, and the peak load. The beam exhibits cracking at a load of 38.01 kN with a bottom flexural reinforcement strain of 0.000 mm/mm, while the 3D-NLFEA model shows no cracking under the same load. At a load of 125.03 kN, the experimental results indicate that the flexural reinforcement yields a strain of 0.0024 mm/mm, whereas the 3D-NLFEA model predicts no yielding, with a strain of 0.0014 mm/mm. At the peak load, the experimental results record a maximum load of 202.36 kN with a strain of 0.0146 mm/mm, compared to the 3D-NLFEA model, which predicts a peak load of 193.92 kN and a strain of 0.0085 mm/mm.
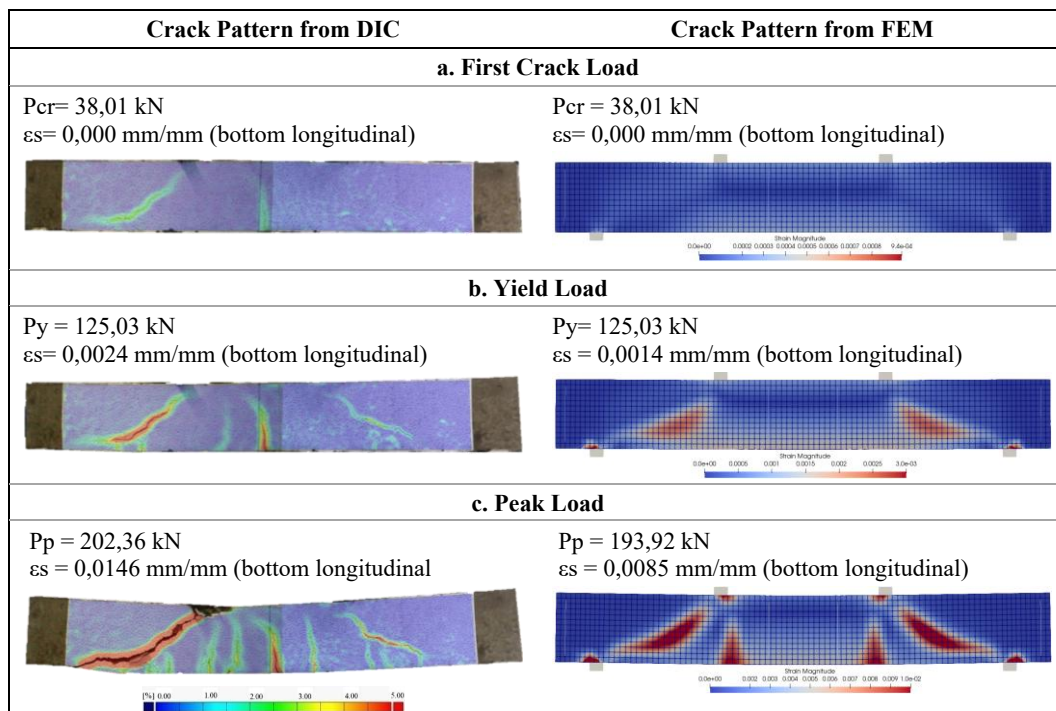

Figure 34. Comparison of crack patterns from DIC analysis and FEM for the G1C2 beam type

The comparison of crack patterns obtained from DIC analysis and FEM applied to a normal concrete beam (PCC) of type P1B2 is shown in Figure 35. As seen in Figure 4.45, the experimental results indicate that the first crack occurs at a load of 29.30 kN, while the 3D-NLFEA finite element model predicts no cracking under the same load, with a strain of 0.000 mm/mm in both cases. The P1B2 beam experiences failure before the bottom flexural reinforcement yields. The failure mode observed in this beam is diagonal tension failure, leading to brittle failure. This occurs at a load of 130.71 kN, with an experimental reinforcement strain of 0.0020 mm/mm. In contrast, the 3D-NLFEA model predicts a reinforcement strain of 0.0021 mm/mm.
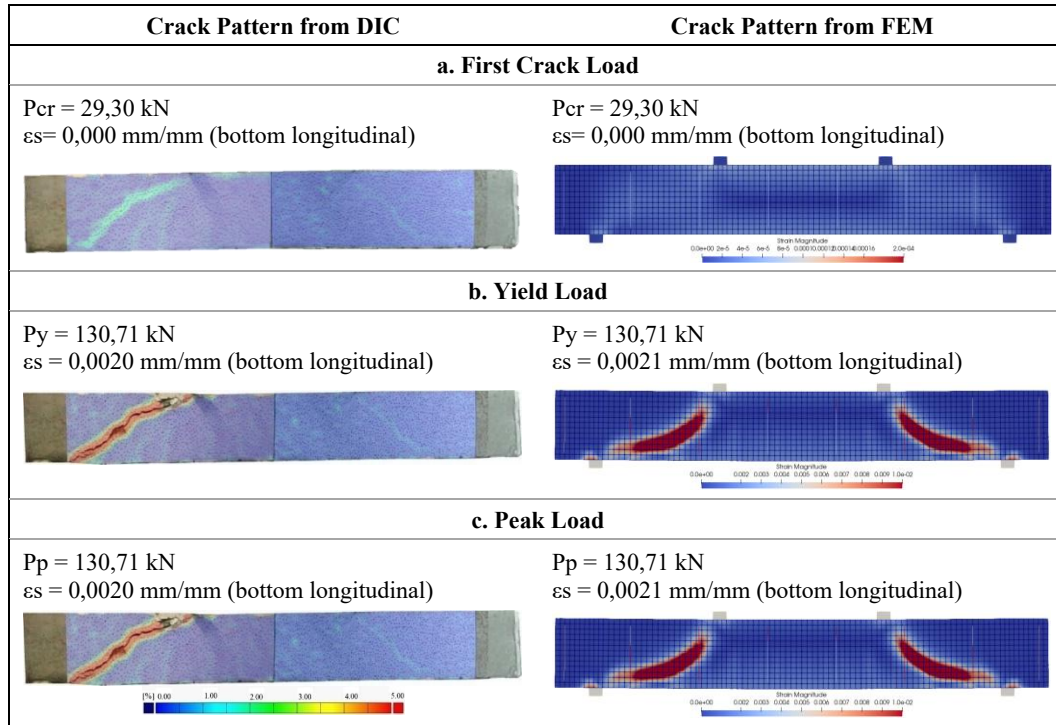
Crack Pattern from DIC	Crack Pattern from FEM
a. First Crack Load	
Pcr = 29,30 kN εs= 0,000 mm/mm (bottom longitudinal)	Pcr = 29,30 kN εs= 0,000 mm/mm (bottom longitudinal)
b. Yield Load	
Py = 130,71 kN εs = 0,0020 mm/mm (bottom longitudinal)	Py = 130,71 kN εs = 0,0021 mm/mm (bottom longitudinal)
c. Peak Load	
Pp = 130,71 kN εs = 0,0020 mm/mm (bottom longitudinal)	Pp = 130,71 kN εs = 0,0021 mm/mm (bottom longitudinal)

Figure 35. Comparison of crack patterns from DIC analysis and FEM for the P1B2 beam type

The comparison of crack patterns from DIC analysis and FEM, presented in Figures 30 to 35, reveals no significant differences. The finite element model exhibits behavior consistent with the results obtained from DIC analysis.

4. Conclusions

This study used a dry mixing technique to explore the shear behavior of high calcium fly ash-based ultra-low carbon-reinforced concrete beams. The research tested five ultra-low carbon concrete (ULCC) beam specimen types: G1A2, G1B2, G1B2.5, G2B2, G1C2, and P1B2. These specimens varied in terms of shear reinforcement ratio, flexural reinforcement ratio, and load placement a/d ratio. The study addressed various aspects, including the material testing outcomes and the mix design for ultra-low carbon concrete, experimental observations of the shear behavior of ULCC beams, and a comparison of experimental shear and load capacities with theoretical calculations. Based on these investigations, the following conclusions were drawn:

- This study's ultra-low carbon concrete mix design exceeded the initial expectations based on preliminary calculations. Aimed initially for a strength of 35 MPa, the concrete's actual compressive strength surpassed 50 MPa at 28 days, as revealed by test results.

- The actual compressive strength of Portland cement concrete (PCC) was lower than the values predicted by the mix design calculations. Test results revealed that the PCC achieved a compressive strength of 32.59 MPa, whereas the target strength set during the mix design phase was 35 MPa. Consequently, this disparity in compressive strength between ultra-low carbon concrete (ULCC) and Portland cement concrete (PCC) indicates that the G1B2 and P1B2 type beams are not comparable in peak load, shear capacity, and observed cracking patterns. The lower compressive strength of PCC compared to ULCC can be attributed to challenges faced by the researchers in achieving strength parity between the two concrete types. Therefore, future studies should focus on improving the ULCC mix design to ensure that both PCC and ULCC beams attain similar compressive strengths, enabling more accurate comparisons.

- In an experiment comparing different stirrup spacings, beams G1A2 with 200 mm spacing, G1B2 with 250 mm spacing, and G1C2 without stirrups yielded shear capacities of 104.34 kN, 115.04 kN, and 101.18 kN, respectively.

Surprisingly, the G1B2 beams with wider spacing outperformed the G1A2 beams by 10.25%, despite predictions suggesting tighter stirrups would enhance shear capacity. This anomaly might stem from the different concrete compressive strengths: 51.57 MPa for G1A2 and 58.23 MPa for G1B2. Comparatively, G1C2 beams showed a 12.05% lower shear capacity than G1B2, illustrating the significant role of stirrups in enhancing shear strength.

- The beam specimens have dimensions of 250 mm in height and 150 mm in width. Beam type G1A2 is detailed with a stirrup spacing of 200 mm, whereas beam type G1B2 uses a spacing of 250 mm. The variation in analytical results related to stirrup spacing may not solely be attributed to differences in material strength; it could also be influenced by the relatively small difference in shear reinforcement spacing between the two beam types.

- A comparison of the shear capacity between beams G1B2 and G2B2 highlighted the impact of flexural reinforcement. G1B2 beams, reinforced with 2D16, and G2B2 beams, with 3D16, showed shear capacities of 115.04 kN and 151.01 kN, respectively. This represents a substantial 31.27% increase in capacity for the G2B2 beams, underscoring the importance of higher flexural reinforcement in boosting shear strength.

- Examining the influence of load position on shear capacity, G1B2 beams displayed a shear capacity of 115.04 kN, whereas G1B2.5 beams showed a decreased capacity of 89.00 kN, marking a 22.63% reduction. This indicates that the placement of the load significantly affects shear strength, with a higher a/d value leading to a decrease in capacity and vice versa.

- Comparing the shear capacity of ultra-low carbon concrete (ULCC) beams from experimental tests with calculations per ACI 318-19 standards revealed that the observed shear capacities exceeded those predicted analytically. This discrepancy suggests that the ACI 318-19 calculation method tends to be more conservative than the actual performance observed in experimental conditions.

- Finite element modeling using 3D-NLFEA software produced results closely aligned with the experimental findings regarding load-deflection curves, shear capacity, and observed crack patterns.

- The crack pattern analysis using Digital Image Correlation (DIC) demonstrated results that closely matched the experimental crack patterns. Digital Image Correlation (DIC) analysis effectively detected small crack patterns

5. Declarations

5.1. Author Contributions

Conceptualization, Y.T. and M.S.M.; methodology, M.S.M.; software, M.S.M.; validation, Y.T., P.S., and W.S.; formal analysis, A.K.A.; investigation, M.S.M.; resources, W.S.; data curation, W.S.; writing—original draft preparation, M.S.M.; writing—review and editing, Y.T.; visualization, A.K.A.; supervision, P.S.; project administration, A.K.A.; funding acquisition, Y.T. All authors have read and agreed to the published version of the manuscript.

5.2. Data Availability Statement

The data presented in this study are available in the article.

5.3. Funding and Acknowledgements

5.4. Conflicts of Interest

The authors declare no conflict of interest.

6. References

[1] Rajamane, N. P., Nataraja, M. C., & Lakshmanan, N. (2011). An introduction to geopolymer concrete. Indian Concrete Journal, 85(11), 25–28.

[2] McLellan, B. C., Williams, R. P., Lay, J., Van Riessen, A., & Corder, G. D. (2011). Costs and carbon emissions for geopolymer pastes in comparison to ordinary Portland cement. Journal of Cleaner Production, 19(9–10), 1080–1090. doi:10.1016/j.jclepro.2011.02.010.

[3] Flatt, R. J., Roussel, N., & Cheeseman, C. R. (2012). Concrete: An eco material that needs to be improved. Journal of the European Ceramic Society, 32(11), 2787–2798. doi:10.1016/j.jeurceramsoc.2011.11.012.

[4] Gartner, E., & Hirao, H. (2015). A review of alternative approaches to the reduction of CO_2 emissions associated with the manufacture of the binder phase in concrete. Cement and Concrete Research, 78, 126–142. doi:10.1016/j.cemconres.2015.04.012.

[5] Martínez, J. D. R., Ríos, J. D., Cifuentes, H., & Leiva, C. (2025). Multi-Scale Toughening of UHPC: Synergistic Effects of Carbon Microfibers and Nanotubes. Fibers, 13(4). doi:10.3390/fib13040049.

[6] Zhang, L., Bian, M., Xiao, Z., Wang, Y., Xu, K., Han, B., & Huang, H. (2024). Using nano-$CaCO_3$ and ceramic tile waste to design low-carbon ultra-high performance concrete. Nanotechnology Reviews, 13(1), 20230198. doi:10.1515/ntrev-2023-0198.

[7] hang, G., Chen, Z., & Zheng, Y. (2024). Research on High Toughness Concrete based on Green Ultra-low Carbon. Academic Journal of Science and Technology, 12(1), 329–334. doi:10.54097/wanhfz37.

[8] Ryu, G. S., Lee, Y. B., Koh, K. T., & Chung, Y. S. (2013). The mechanical properties of fly ash-based geopolymer concrete with alkaline activators. Construction and Building Materials, 47, 409–418. doi:10.1016/j.conbuildmat.2013.05.069.

[9] Tajunnisa, Y., Sugimoto, M., Sato, T., Jaya, J., & Shigeishi, M. (2016). Characterization of Low Calcium Fly Ash for Geopolymer Paste. 16th International Conference and Exhibition: Structural Faults & Repair, Scotland, United Kingdom.

[10] Tajunnisa, Y., Sugimoto, M., Sato, T., & Shigeishi, M. (2017). A study on factors affecting geopolymerization of low calcium fly ash. International Journal of GEOMATE, 13(36), 100–107. doi:10.21660/2017.36.84153.

[11] Glasby, T., Day, J., Genrich, R., & Kemp, M. (2015). Commercial Scale Geopolymer Concrete Construction. The Saudi International Building and Constructions Technology Conference, 26-29 October, 2015, Riyadh, Saudi Arabia.

[12] Glasby, T., Day, J., Genrich, R., & Aldred, J. (2015). EFC geopolymer concrete aircraft pavements at Brisbane West Wellcamp Airport. 27th Biennial National Conference of the Concrete Institute of Australia (CIA), 30 August - 2 September, Melbourne, Australia.

[13] Ma, C. K., Awang, A. Z., & Omar, W. (2018). Structural and material performance of geopolymer concrete: A review. Construction and Building Materials, 186, 90–102. doi:10.1016/j.conbuildmat.2018.07.111.

[14] Sujatha, T., Kannapiran, K., & Nagan, S. (2012). Strength assessment of heat cured geopolymer concrete slender column. Asian Journal of Civil Engineering, 13(5), 635–646.

[15] Albitar, M., Mohamed Ali, M. S., & Visintin, P. (2017). Experimental study on fly ash and lead smelter slag-based geopolymer concrete columns. Construction and Building Materials, 141, 104–112. doi:10.1016/j.conbuildmat.2017.03.014.

[16] Rahman, M., & Sarker, P. K. (2011). Geopolymer concrete columns under combined axial load and biaxial bending. In Proceedings of the Concrete 2011 Conference, 12 October, Perth, Australia.

[17] Sumajouw, M. D. J., & Rangan, B. V. (2006). Low-calcium fly ash-based geopolymer concrete: reinforced beams and columns. Research Report GC 3, Curtin University of Technology, , Perth, Australia.

[18] Ganesan, N., Abraham, R., Raj, S. D., & Namitha, K. (2016). Effect of fibres on the strength and behaviour of GPC columns. Magazine of Concrete Research, 68(2), 99–106. doi:10.1680/jmacr.15.00049.

[19] Nagan, S., & Karthiyaini, S. (2014). A study on load carrying capacity of fly ash based polymer concrete columns strengthened using double layer GFRP wrapping. Advances in Materials Science and Engineering, 2014. doi:10.1155/2014/312139.

[20] Al-Mashhadani, M. M., Canpolat, O., Aygörmez, Y., Uysal, M., & Erdem, S. (2018). Mechanical and microstructural characterization of fiber reinforced fly ash based geopolymer composites. Construction and building materials, 167, 505-513. doi:10.1016/j.conbuildmat.2018.02.061.

[21] Devika, C. P., & Deepthi, R. (2015). Study of flexural behavior of hybrid fibre reinforced geopolymer concrete beam. In International Journal of Science and Research, 4(7), 130-135.

[22] Nagan, S., & Mohana, R. (2014). Behaviour of geopolymer ferrocement slabs subjected to impact. Iranian Journal of Science and Technology. Transactions of Civil Engineering, 38(C1+), 223.

[23] Rajendran, M., & Soundarapandian, N. (2013). An experimental investigation on the flexural behavior of geopolymer ferrocement slabs. Journal of Engineering and Technology, 3(2), 97. doi:10.4103/0976-8580.113047.

[24] Visintin, P., Mohamed Ali, M. S., Albitar, M., & Lucas, W. (2017). Shear behaviour of geopolymer concrete beams without stirrups. Construction and Building Materials, 148, 10–21. doi:10.1016/j.conbuildmat.2017.05.010.

[25] Yacob, N. S., ElGawady, M. A., Sneed, L. H., & Said, A. (2019). Shear strength of fly ash-based geopolymer reinforced concrete beams. Engineering Structures, 196. doi:10.1016/j.engstruct.2019.109298.

[26] Darmawan, M. S., Bayuaji, R., Sugihardjo, H., Husin, N. A., & Affandhie, R. B. A. (2019). Shear strength of geopolymer concrete beams using high calcium content fly ash in a marine environment. Buildings, 9(4), 98. doi:10.3390/buildings9040098.

[27] Yost, J. R., Radlińska, A., Ernst, S., Salera, M., & Martignetti, N. J. (2013). Structural behavior of alkali activated fly ash concrete. Part .Structural testing and experimental findings. Materials and Structures/Materiaux et Constructions, 46(3), 449–462. doi:10.1617/s11527-012-9985-0.

[28] Darmawan, M. S., Tajunnisa, Y., Suprobo, P., Sutrisno, W., & Aziz, M. W. (2022). Comparative Study of Flexural Performance of Geopolymer and Portland Cement Concrete Beam Using Finite Element Analysis. International Journal of GEOMATE,. 23(95), 1-9. doi:10.21660/2022.95.j2340.

[29] Tambusay, A., Suryanto, B., & Suprobo, P. (2020). Nonlinear finite element analysis of reinforced concrete beam-column joints under reversed cyclic loading. IOP Conference Series: Materials Science and Engineering, 930(1), 012055. doi:10.1088/1757-899X/930/1/012055.

[30] Chong, K., Suryanto, B., Tambusay, A., & Suprobo, P. (2022). Nonlinear Analysis of Reinforced Geopolymer Concrete Beams. Civil Engineering Dimension, 24(1), 1–10. doi:10.9744/ced.24.1.1-10.

[31] Tambusay, A., Suprobo, P., Suryanto, B., & Don, W. (2021). Application of nonlinear finite element analysis on shear-critical reinforced concrete beams. Journal of Engineering and Technological Sciences, 53(4). doi:10.5614/j.eng.technol.sci.2021.53.4.8.

[32] Antoni, A., Wijaya, S. W., Satria, J., Sugiarto, A., & Hardjito, D. (2016). The Use of Borax in Deterring Flash Setting of High Calcium Fly Ash Based Geopolymer. Materials Science Forum, 857, 416–420. doi:10.4028/www.scientific.net/msf.857.416.

[33] Topark-Ngarm, P., Chindaprasirt, P., & Sata, V. (2015). Setting Time, Strength, and Bond of High-Calcium Fly Ash Geopolymer Concrete. Journal of Materials in Civil Engineering, 27(7), 04014198. doi:10.1061/(asce)mt.1943-5533.0001157.

[34] Bayuaji, R., Yasin, A. K., Susanto, T. E., & Darmawan, M. S. (2017). A review in geopolymer binder with dry mixing method (geopolymer cement). AIP Conference Proceedings, 1887. doi:10.1063/1.5003505.

[35] Mo, Z., Li, C., Zhang, W., Liu, C., Sun, Y., Liu, R., & Lu, X. (2024). Cryogenic Digital Image Correlation as a Probe of Strain in Iron-Based Superconductors. Chinese Physics Letters, 41(10), 107102. doi:10.1088/0256-307X/41/10/107102.

[36] Wubalem, A., Caselle, C., Taboni, B., & Umili, G. (2025). Effects of Rock Texture on Digital Image Correlation. Geosciences (Switzerland), 15(4), 145. doi:10.3390/geosciences15040145.

[37] Zhang, D., Huang, G., Li, L., He, S., Su, Y., Huang, S., Jiang, M., & Wang, W. (2025). Preprocessing methods for reducing the impact of image decorrelation in laser speckle digital image correlation. Optics Continuum, 4(3), 476–487. doi:10.1364/OPTCON.542356.

[38] Tong, Z., Frolkin, D., Shi, H., LaRue, T., Rausch, M., & Yang, J. (2024). 3D Stereo Adaptive Mesh Augmented Lagrangian Digital Image Correlation. Research Square, 1-41. doi:10.21203/rs.3.rs-5507109/v1.

[39] Phoo-Ngernkham, T., Phiangphimai, C., Damrongwiriyanupap, N., Hanjitsuwan, S., Thumrongvut, J., & Chindaprasirt, P. (2018). A Mix Design Procedure for Alkali-Activated High-Calcium Fly Ash Concrete Cured at Ambient Temperature. Advances in Materials Science and Engineering, 2460403. doi:10.1155/2018/2460403.

[40] Xie, T., Visintin, P., Zhao, X., & Gravina, R. (2020). Mix design and mechanical properties of geopolymer and alkali activated concrete: Review of the state-of-the-art and the development of a new unified approach. Construction and Building Materials, 256. doi:10.1016/j.conbuildmat.2020.119380.

[41] Chindaprasirt, P., Boonbamrung, T., Poolsong, A., & Kroehong, W. (2021). Effect of elevated temperature on polypropylene fiber reinforced alkali-activated high calcium fly ash paste. Case Studies in Construction Materials, 15, e00554. doi:10.1016/j.cscm.2021.e00554.

[42] Husin, N. A., Bayuaji, R., Tajunnisa, Y., Darmawan, M. S., & Suprobo, P. (2020). Performance of high calcium fly ash based geopolymer concrete in chloride environment. International Journal of GEOMATE, 19(74), 107–113. doi:10.21660/2020.74.56966a.

[43] Piscesa, B., Attard, M. M., Prasetya, D., & Suprobo, P. (2019). Finite element analysis of the Circular Double Skin Tubular Concrete (DSTC) under concentric loading. MATEC Web of Conferences, 276, 01009. doi:10.1051/matecconf/201927601009.

[44] Piscesa, B., Attard, M. M., & Samani, A. K. (2014). Refined plasticity model for concrete stress-strain relationship part I: prediction of peak stress and residual stress. 23rd Australasian Conference on the Mechanics of Structures and Materials (ACMSM23), 9-12 December, 2014, Byron Bay, Australia.

[45] Li, Z. J., Balendra, T., Tan, K. H., & Kong, K. H. (2005). Finite element modeling of cyclic behavior of shear wall structure retrofitted using GFRP. ACI Special Publication, 230(74), 1350-1324.

[46] Piscesa, B., Attard, M. M., & Samani, A. K. (2017). Plastic dilation rate characteristic of concrete confined with steel tube. COMPLAS XIV: proceedings of the XIV International Conference on Computational Plasticity: fundamentals and applications (CIMNE), . 5-7 September, 2017, Barcelona, Spain.

[47] Piscesa, B., Attard, M. M., & Samani, A. K. (2014). Refined plasticity model for concrete stress-strain relationship part II: inclusion of size effect. 23rd Australasian Conference on The Mechanics of Structures and Materials (ACMSM23), 9-12 December, 2014, Bryon Bay, Australia.

[48] Piscesa, B., Attard, M. M., Samani, A. K., & Tangaramvong, S. (2017). Plasticity constitutive model for stress-strain relationship of confined concrete. ACI Materials Journal, 114(2), 361–371. doi:10.14359/51689428.

[49] Piscesa, B., Alrasyid, H., Prasetya, D., & Iranata, D. (2021). Numerical Investigation of Reinforced Concrete Beam Due to Shear Failure. IPTEK The Journal for Technology and Science, 31(3), 373. doi:10.12962/j20882033.v31i3.7385.

[50] Bentz, E. (2000). Sectional analysis of reinforced concrete members. Ph.D. Thesis, University of Toronto, Toronto, Canada.

[51] Vecchio, F. J., & Shim, W. (2004). Experimental and Analytical Reexamination of Classic Concrete Beam Tests. Journal of Structural Engineering, 130(3), 460–469. doi:10.1061/(asce)0733-9445(2004)130:3(460).